

New black hole mergers in the LIGO–Virgo O3 data from a gravitational wave search including higher-order harmonics

Digvijay Wadekar,^{1,*} Javier Roulet,² Tejaswi Venumadhav,^{3,4} Ajit Kumar Mehta,³
Barak Zackay,⁵ Jonathan Mushkin,⁵ Seth Olsen,⁶ and Matias Zaldarriaga¹

¹*School of Natural Sciences, Institute for Advanced Study, 1 Einstein Drive, Princeton, NJ 08540, USA*

²*TAPIR, Walter Burke Institute for Theoretical Physics,
California Institute of Technology, Pasadena, CA 91125, USA*

³*Department of Physics, University of California at Santa Barbara, Santa Barbara, CA 93106, USA*


⁴*International Centre for Theoretical Sciences, Tata Institute of Fundamental Research, Bangalore 560089, India*

⁵*Department of Particle Physics & Astrophysics, Weizmann Institute of Science, Rehovot 76100, Israel*

⁶*Department of Physics, Princeton University, Princeton, NJ 08540, USA*

(Dated: December 12, 2023)

Nearly all of the previous gravitational wave (GW) searches in the LIGO–Virgo data included GW waveforms with only the dominant quadrupole harmonic, i.e., omitting higher-order harmonics which are predicted by general relativity. Based on the techniques developed in Wadekar *et al.* [1, 2], we improve the IAS pipeline by (i) introducing higher harmonics in the GW templates, (ii) downweighting noise transients (“glitches”) to improve the search sensitivity to high-mass and high-redshift binary black hole (BBH) mergers. We find 14 new candidate BBH mergers with $0.53 \leq p_{\text{astro}} \leq 0.88$ on running our pipeline over the public LIGO–Virgo data from the O3 run (we use the detection threshold as the astrophysical probability, p_{astro} , being over 0.5, following the approach of other pipelines). We also broadly recover the high-significance events from earlier catalogs, except some which were either vetoed or fell below our SNR threshold for trigger collection.

A few notable properties of our new candidate events are as follows. At $> 95\%$ credibility, 4 candidates have total masses in the intermediate-mass black hole (IMBH) range (i.e., above $100 M_{\odot}$), and 9 candidates have redshifts $z > 0.5$. 9 candidates have median mass of the primary BH falling roughly within the pair instability mass gap, with the highest primary mass being $300_{+60}^{-120} M_{\odot}$. 5 candidates have median mass ratio $q < 0.5$. Under a prior uniform in effective spin χ_{eff} , 6 candidates have $\chi_{\text{eff}} > 0$ at $> 95\%$ credibility. We also find that including higher harmonics in our search raises the significance of a few previously reported marginal events (e.g., GW190711_030756). While our new candidate events have modest false alarm rates ($\gtrsim 1.6/\text{yr}$), a population inference study including these can better inform the parameter space of BHs corresponding to the pair instability mass gap, high redshifts, positive effective spins and asymmetric mass ratios. 

I. INTRODUCTION

Gravitational waves (GW) from roughly 100 binary black hole (BBH) mergers have been detected in the data from the first three observing runs of the LIGO–Virgo–Kagra collaboration (LVK), combining detections by the LVK [3–7] and by other independent pipelines [8–15] who access the data made publicly available through the Gravitational Wave Open Science Center (GWOSC) [16]. Nearly all the previous template-bank based searches have approximated GW waveforms to have only the dominant quadrupole mode, $(\ell, |m|) = (2, 2)$, where the frequency of GWs is twice the orbital frequency.

The (2, 2) mode appears at the lowest order in post-Newtonian (PN) expansion, but there are a number of higher harmonics originating from the subsequent orders of the PN expansion (e.g., the (3, 3) mode has thrice the orbital frequency) [18, 19]. Approximate formulae for the relative strength of frequency-domain amplitudes of two

of the higher-order modes (HM) are given by [1]

$$\begin{aligned} \frac{A_{33}(3f)}{A_{22}(2f)} &\simeq \frac{3\sqrt{5}}{2\sqrt{7}} \left[\frac{1-q}{1+q} \right] (2\pi M_{\text{tot}} f)^{1/3} \sin \iota \\ \frac{A_{44}(4f)}{A_{22}(2f)} &\simeq \frac{8\sqrt{10}}{9\sqrt{7}} \left[1 - \frac{3q}{(1+q)^2} \right] (2\pi M_{\text{tot}} f)^{2/3} \sin^2 \iota \end{aligned} \quad (1)$$

where q is the mass ratio ($= m_2/m_1$), f is the orbital frequency and ι is the binary inclination ($\iota = \pi/2$ corresponds to the edge-on configuration). These harmonics have a number of important applications for characterizing properties of BBHs. If one uses the (2, 2) mode waveform alone in inferring the BBH properties, we have the following important degeneracies between different binary parameters: luminosity distance and ι ; q and effective spin (χ_{eff}); polarization and initial orbital phase (ϕ_{initial}). All three degeneracies are broken by HM [20, 21]. This follows from the amplitudes of HM having a different dependence on ι and q as compared to that of the (2, 2) mode (see Eq. (1)), and similarly the phases of HM have different dependence on ϕ_{initial} . It is worth mentioning that the degeneracy between distance and inclination is currently one of the most important limiting factors in inferring the Hubble parameter H_0 from GW

* jayw@ias.edu

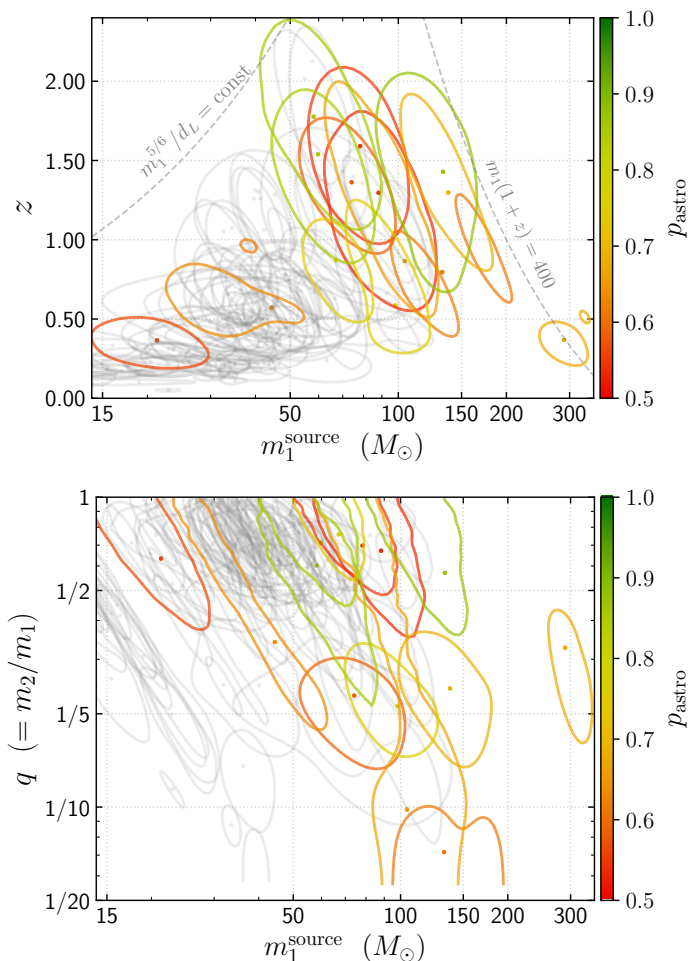


FIG. 1. The source-frame total mass and effective spin (mass ratio) for events are shown in the top (bottom) panels. In colored contours, we show properties of the 14 new candidate events found in our O3 search with $p_{\text{astro}} > 0.5$ (p_{astro} is the probability of events being of astrophysical origin, as opposed to being a noise transient). The color of the contours corresponds to p_{astro} values of the events. All the previously reported events from O1–O3 runs (combining the GWTC-3 LVK catalog, the OGC-4 catalog and the previous IAS catalogs) are shown in transparent gray contours [3, 4, 6–10]. The posterior contours are obtained from parameter estimation runs using *cogwheel* [17] and enclose 50% of the probability and median values are represented by dots. The dashed lines in the upper panel give a rough indication of the limits of our search under the current detector sensitivity, see the text in Section III A 1 for further details. Interestingly, some of the new candidate events have support in the ranges corresponding to IMBH masses, pair-instability mass gap, high redshift, and low mass ratio.

systems and HM can be crucial in breaking this degeneracy. Similarly, events which have HM also have the best measured mass ratios (e.g., [22, 23]). HM become important in the strong gravity regime close to merger and are thus useful to test the multipolar structure of gravity [24–28], and to study properties of the merger remnant

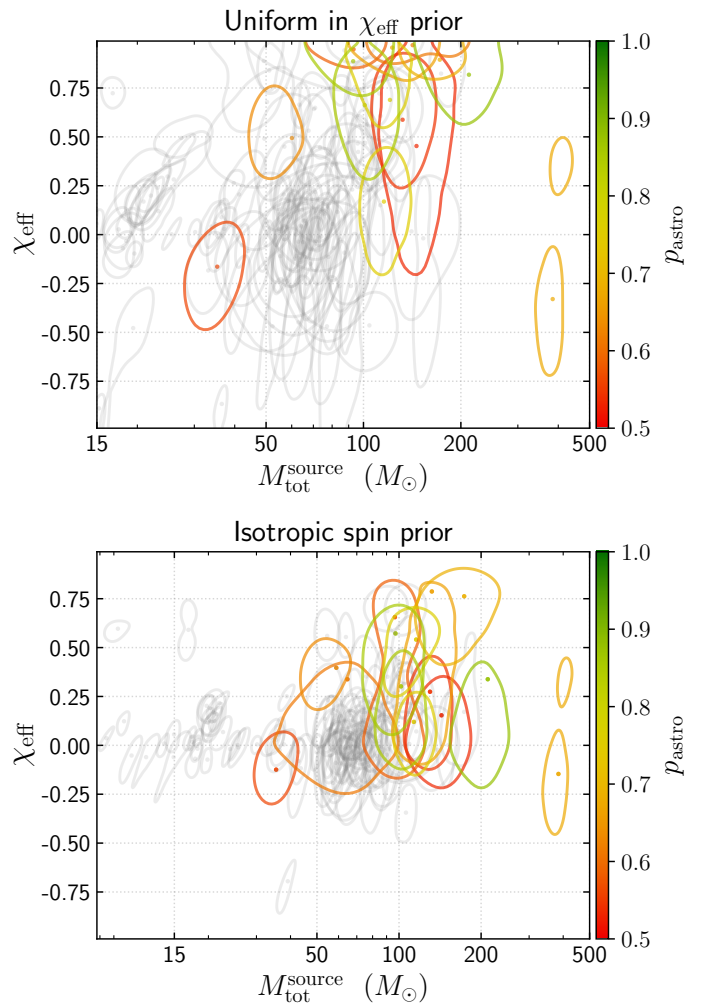


FIG. 2. Same as Fig. 1, but for the total mass and the effective spin. **Top:** Uniform prior on χ_{eff} (which is the fiducial prior adopted throughout this paper). **Bottom:** Results with isotropic priors on individual spins (which favors χ_{eff} closer to zero), which is also used in the GWTC-3 and 4-OGC catalogs. The relative significance for positive χ_{eff} values indeed decreases in the isotropic prior, but there are a few events which still show preference for positive χ_{eff} . To determine whether this preference is due to positive χ_{eff} systems having larger power in the detector band (particularly in the high-mass case, see Fig. 6), or if the preference is an intrinsic property of the sources, we plan to do an injection study in the future. We show similar plots for $\chi_{\text{eff}}-q$ and $\chi_{\text{eff}}-z$ combinations in Fig. 7 in the Appendix.

such as the recoil kick.

Multiple waveform models including HM have been recently made available [29–31], and they are currently being used ubiquitously in parameter estimation studies. However, *HM are still not included in current search pipelines* (as of now, the only exception is Ref. [32], which searched for binaries with nearly edge-on inclinations). The reason behind this is that for making template banks with the (2, 2) mode, one only needs to sample over the

masses and spins of black holes $(m_1, m_2, \chi_1, \chi_2)$. However, for constructing banks including HM, one needs to additionally sample over the inclination and initial phase $(\iota, \phi_{\text{initial}})$. These additional degrees of freedom can cause: (i) the size of the template banks and the cost of search to increase significantly (by a factor of ~ 100 for the case of HM [32–34]), (ii) loss of sensitivity in the search as there is increased number of background triggers [35]. To tackle the first issue, we found more efficient ways of including HM in our template banks (which we presented in detail in our first companion paper [1]). Regarding the second issue, we devise new detection statistics which includes marginalization over the amplitudes and phases of higher modes in our second companion paper [2]. We present an overview of these new techniques in Section II.

We see from Eq. (1) that, at a given orbital frequency, the relative HM amplitudes increase as a power-law with M_{tot} . Moreover, due to the shape of the current detector power spectral density (PSD), the signal-to-noise ratio (SNR) contribution of HM is additionally boosted at high masses and redshifts. In this regime, the (2, 2) mode can cut off below the detector’s sensitive band (the detector PSD sharply increases below ~ 100 Hz) and HM, being at higher frequencies, naturally have an increased contribution to the SNR. The background corresponding to the high-mass regime is however heavily dominated by short-duration noise transients (called instrumental “glitches”). This is because the high-mass waveforms have a very short duration in band, which makes it easy for transients like blip glitches to mimic real signals. We therefore introduce additional methods in the IAS pipeline to downweight the background at high masses. These methods are detailed in our second companion paper [2] and we present an overview in Section II C.

Running our new search pipeline over the public LIGO–Virgo data from the third observing run (O3), we found new candidate events with properties shown in Figs. 1 and 2. We further discuss these new events and also show our search results for the events from the GWTC-3 and 4-OGC catalogs in Section III. We review the interesting astrophysical properties of the new candidate events in Section IV. We analyze the impact of our astrophysical prior and comment upon the gain/loss of sensitivity due to adding HM in Section V, and we conclude in Section VI.

II. PIPELINE IMPROVEMENTS

Here, we present an outline of the additions that we made to the (2, 2)-only IAS pipeline [8, 10].

A. Adding HM in template banks

In this sub-section, we summarize the methodology for constructing template banks for HM from our com-

panion paper: Wadekar *et al.* [1]. For each (2, 2) mode template, we use a combination of post-Newtonian formulae and machine learning tools to model normalized aligned-spin templates corresponding to the (3, 3) and (4, 4) modes. We then filter the data separately with the three templates and store the complex SNR timeseries $(\rho_{22}, \rho_{33}, \rho_{44})$, see figure 1 of [1]. As a result, our HM search matched-filtering cost is just $3\times$ that of a (2, 2)-only search (in contrast to being $\sim 100\times$ as in previous HM search methods, where the different modes are combined and templates sample over inclination and initial orbital phase [32–34]).

We divide our search space into 17 template banks, which are divided according to the shape of normalized (2, 2) waveforms corresponding to the binary parameters (the shape of normalized waveforms is roughly related to the binary merger frequency). The parameter space corresponding to each bank is shown in the bottom panel of Fig. 8 in the Appendix. Some of the banks are further divided into subbanks based on the range of chirp masses they cover. Note that the division into banks and subbanks is only to facilitate covering the parameter space with templates of the form that we use, and the final ranking statistic we assign to each trigger is weighed against those of all other triggers (over the entire parameter space) to estimate its global significance. Other than adding HM, we also improved our (2, 2) template banks by using a machine learning tool called random forest regressor (which helps us reduce the dimensionality of our template banks and enables us to search with 30–40% fewer templates than before) [1].

B. New statistics for combining SNR timeseries from different harmonics

We present the techniques for combining the $(\rho_{22}, \rho_{33}, \rho_{44})$ timeseries in our companion paper (Wadekar *et al.* [2]) and here we provide a brief overview. Combining SNR timeseries of different modes incorrectly can lead to a large loss of sensitivity of the pipeline [35]. We use the Neyman–Pearson lemma to develop an optimal statistic to combine the SNR timeseries for different harmonics; our detection statistic is the ratio of the Bayesian evidence under the signal and the noise hypothesis. Ideally, one would marginalize over all the intrinsic and extrinsic binary parameters to calculate the evidence under the signal hypothesis. We develop two different approximate versions of the statistic to be used in different parts of our pipeline as detailed in the sub-sections below.

1. Single-detector marginalized statistic

We first developed an approximate statistic to collect individual detector triggers. Similar to other pipelines, we set a particular SNR threshold (ρ_{collect}) to collect triggers from individual detectors. The primary reason be-

hind this is to reduce the number of triggers passed to the next steps of the pipeline (coincidence analysis, veto and coherent score calculation) as these steps are computationally expensive (another reason is storage space constraints when saving a large number of triggers on disk). For collecting the triggers in a (2, 2)-only search, one can simply use $|\rho_{22}|^2 > \rho_{\text{collect}}^2$. For the HM case, if we naively use $|\rho_{22}|^2 + |\rho_{33}|^2 + |\rho_{44}|^2 > \rho_{\text{collect}}^2$, the number of collected triggers increases by a factor of over 100 (using the same value of ρ_{collect} as the (2, 2)-only case [2]). To ameliorate this, we develop in Ref. [2] a new marginalized statistic (ρ_{HM}) which exploits the fact that the values of $|\rho_{33}/\rho_{22}|$ and $|\rho_{44}/\rho_{22}|$ are bounded for physical signals (as opposed to Gaussian noise triggers where the values $|\rho_{33}/\rho_{22}|$ and $|\rho_{44}/\rho_{22}|$ can be arbitrarily large). The statistic ρ_{HM} includes marginalization over physically possible amplitude ratios of higher harmonics. To make the computation of ρ_{HM} faster, we maximize (instead of marginalizing) over the phases of HM and also over all the remaining intrinsic and extrinsic binary parameters (although this can be improved in future studies). We collect single-detector triggers using $\rho_{\text{HM}}^2 > \rho_{\text{collect}}^2$ and we use a larger value of the collection threshold as compared to the (2, 2)-only case. The downside of increasing the value of ρ_{collect} is that low-SNR events can fall below our threshold bar. This is indeed the reason behind our pipeline missing some of the low-SNR events reported by (2, 2)-only pipelines in the previous literature, see Section III C below for more details. The particular choice of ρ_{collect} that we made in the current paper is currently not a bottleneck for our search and can be improved in the future.

2. Coherent marginalized statistic

Once we collect single detector triggers, we check if the same template(s) fired in other detectors at a similar time. To rank the resulting coincident triggers (for calculating their false-alarm rate (FAR) and subsequently p_{astro}), we develop a more accurate statistic which also includes coherence between different detectors for ranking the events. For example, we exploit the fact that astrophysical signals have correlated phase and time differences between the detectors, while the noise triggers have random distributions [36]. In the previous subsection, we maximized over extrinsic binary parameters, but marginalizing over them is the more optimal strategy. Our coherent ranking statistic thus includes marginalization over extrinsic parameters in a similar way to the IAS (2, 2)-only search methodology given in Appendix D of Olsen *et al.* [10] (hereafter O22) except generalized to account for higher modes. In addition, we also include marginalization over the amplitude of HM (which effectively corresponds to marginalizing over mass ratios); the only parameters that we currently do not marginalize over are the intrinsic binary parameters corresponding to the 22 waveform, as we use only the best-fit 22 tem-

plate in our calculations. Details regarding our coherent statistic will be given in upcoming papers [2, 37].

C. Removing/downweighting noise transients

In addition to the changes involving higher modes, we also improve the sensitivity of our search for high masses compared to previous IAS pipelines by developing new tools. We also discuss in this sub-section methods to tailor the background reduction techniques in our (2, 2)-only pipeline for the case of HM.

1. Band eraser tool for data preprocessing

In our (2, 2)-only pipeline, in a data pre-processing step (before we matched-filter with templates), we identify regions of bad data segments which have excess power localized to particular frequency ranges and timescales (see section C of [8]). We then remove the data in the flagged regions (i.e., make “holes”) and then fill the holes using an “inpainting filter” (see figure 6 of [38]). Note that the holes remove the entire data from a particular time chunk. Sometimes, however, the noise transients are only localized to particular frequency bands (particularly the low-frequency end $\lesssim 100$ Hz) and do not affect astrophysical signals which dominantly have power in a different frequency band.

Therefore, before making holes in entire time-chunks, we try to smoothly remove bad time-frequency regions (or bands) in the spectrogram. For this, we develop a new tool we call *band eraser*. We divide the spectrogram into multiple bands (each with dimensions $64\text{ s} \times 2\text{ Hz}$). We further split each band into multiple chunks (of $2\text{ s} \times 0.5\text{ Hz}$) and measure the number of chunks which have power above a certain threshold. If this number is above a certain threshold, we remove the entire band from our analysis. We calculate this threshold using Poisson statistics, making sure that, on average, in Gaussian noise, one band is removed per $\sim 4 \times 10^4\text{ s}$ (we also add an additional safety factor to the threshold to avoid removing gravitational wave signals).

We also noticed that some of the noise transients had power spread over long timescales ($\gtrsim 10\text{ s}$) and thus were sometimes missed by the localized excess-power tests (with timescales $\lesssim 1\text{ s}$) that we had used earlier to identify regions for making holes (see Table II of [8]). Empirically, we noticed that such disturbances predominantly pollute the low-frequency ($\lesssim 100\text{ Hz}$) end, and therefore particularly reduced the sensitivity of our pipeline to high-mass mergers. We find that using the band eraser also helped in mitigating some such disturbances. We leave further discussion of the band eraser tool to Ref. [2].

2. Veto procedure

The (2,2)-only IAS pipeline included a series of signal consistency checks in order to veto triggers that are likely to arise from noise transients, in order to improve the search sensitivity (see section I of [8]). On the coincident triggers, we perform similar veto procedures as the (2,2)-only pipeline, except for the following change. For a particular trigger, we first subtract our best-fit (3,3) and (4,4) waveforms from data and then run the same (2,2) signal consistency tests as earlier on the residual data. In the limit in which the higher harmonics are nearly orthogonal to the (2,2) waveform, the consistency tests can be left largely unchanged. We aim to modify these tests to also check the consistency of the (3,3) and (4,4) parts of the signals in the future.

In previous quadrupole-only searches, we reduced the noise background by accounting for the non-stationarity of the PSD [38]. In the procedure, we match-filtered a reference template from the bank with the data and registered its SNR $\rho(t)$. We then estimated the variation in PSD as a function of time by averaging the power $\langle \rho^2 \rangle$ within rolling windows of length ~ 15 s. In this search, we calculate the correction for the PSD drift in the same way as before by only using (2,2) waveforms from our template bank (and not including HM waveforms). In the limit in which the fluctuations of the PSD are described by a scalar over all frequencies, this procedure returns an unbiased estimate of the drift correction.

3. Ranking statistic

Even after performing the above steps, there are still some noise triggers which survive. We use the ranking statistic as a final tool to downweight such triggers. Beyond upweighting triggers which have good coherence among multiple detectors, an important job of the ranking statistic is to also downweight triggers based on the probability with which similar triggers occur in the background. We simulate 2000 instances of background runs using the method of timeslides (where we shift one of the detectors by unphysical amounts which are more than the light crossing time between the detectors).

In the (2,2)-only case, for a trigger with SNR ρ_{22} associated with a template α , this probability under the noise hypothesis \mathcal{N} is $P(|\rho_{22}|^2 | \alpha, \mathcal{N})$. In the case of Gaussian noise, $|\rho_{22}|^2$ follows a $\chi^2_{2 \text{ d.o.f}}$ (i.e., $P(|\rho_{22}|^2 | \alpha, \mathcal{N}) \propto \exp(-|\rho_{22}|^2/2)$). However, we empirically measure $P(|\rho_{22}|^2 | \alpha, \mathcal{N})$ by constructing a histogram of the $|\rho_{22}|^2$ values of background triggers associated with the template α . In our previous papers, we labelled this term as the ‘‘rank function’’ ($\tilde{\rho} \equiv -2 \log P(|\rho_{22}|^2 | \alpha, \mathcal{N})$), see section J of Ref. [8].

In a similar way for the HM case, if the noise were Gaussian, $|\rho_{22}|^2, |\rho_{33}|^2, |\rho_{44}|^2$ separately follow $\chi^2_{2 \text{ d.o.f}}$ distributions (note that we orthogonalize templates of different harmonics), and their sum thus follows a $\chi^2_{6 \text{ d.o.f}}$

distribution with 6 d.o.f. This motivated us to make the approximation $P(\rho_{22}, \rho_{33}, \rho_{44} | \alpha, \mathcal{N}) \propto P(|\rho_{22}|^2 + |\rho_{33}|^2 + |\rho_{44}|^2 | \alpha, \mathcal{N})$ and again measure this probability distribution empirically by constructing a 1D histogram of $(|\rho_{22}|^2 + |\rho_{33}|^2 + |\rho_{44}|^2)$ values of background triggers associated with the template α . We plan to explore beyond the current assumption in a future study.

Note that in the previous IAS studies, $P(|\rho_{22}|^2 | \alpha, \mathcal{N})$ is assumed to be the same for all templates in a sub-bank. However, especially for high masses, this term can have different values even for different templates within a subbank, see e.g., [2, 36, 39]. In order to optimize our analysis, we follow the technique in Ref. [2], where we first cluster the templates within each sub-bank based on their sensitivity to glitches (as quantified empirically by the relative fraction of loud and faint triggers belonging to each template). We then separately construct the histograms of background triggers for each template group to estimate the noise probabilities of triggers associated to templates within that group.

In a future paper, we plan to quantify the improvement in volume-time sensitivity due to the background reduction procedures outlined in this section, by injecting simulated gravitational-wave signals in the data and comparing the fraction of injections recovered by our pipeline.

D. Astrophysical prior

In this section, we discuss the astrophysical prior used in our search. This prior is used to assign weights to different templates according to the probability of the template α firing under the signal hypothesis \mathcal{S} : $P(\alpha | \mathcal{S})$, and also to downweight triggers with unphysical $|\rho_{33}/\rho_{22}|$ and $|\rho_{44}/\rho_{22}|$ ratios as discussed earlier in Section II B.

We only probe binary black hole (BBH) mergers in our study and leave the search for systems containing neutron stars for future work. The range of our search was restricted to the following space:

$$\begin{aligned} 3 M_{\odot} < m_2^{\text{det}} < m_1^{\text{det}} < 400 M_{\odot} \\ 1/18 < q < 1 \\ |\chi_1|, |\chi_2| < 0.99 \end{aligned} \quad (2)$$

where $m^{\text{det}} = m^{\text{source}}(1+z)$ refer to detector-frame (redshifted) masses of the binary. We chose the location of the mass ratio cut for BBHs to restrict to the calibration regime of the IMRPhenomXAS approximant [41], while the cut on the individual spins is due to the relativistic Kerr limit.

We picked a simple prior which broadly covers the parameter space (picking a broad prior can help with reweighting the results to a different prior in the future). Our prior on the mass ratio q is a uniform one on $\log q$ for $1/18 < q < 1$; the effective spin parameter χ_{eff} is flat within $-0.95 < \chi_{\text{eff}} < 0.95$ (with $|\chi_1|, |\chi_2| < 0.99$); the total mass M_{tot} is distributed in a power-law fashion, $P(M_{\text{tot}}) \propto M_{\text{tot}}^{-2}$. Note that we use a prior on the

TABLE I. Properties of new candidate events found in our search with $p_{\text{astro}} > 0.5$. We also report the inverse false-alarm rate (IFAR) and $\rho_{\text{H,L}}$ denotes the incoherent SNR of the triggers in the Hanford and Livingston detectors ($\rho_{\text{H,L}}$ values here include contributions from all harmonics, their separate contributions are shown separately in Table V). The parameter estimation (PE) results are obtained using the IMRPhenomXODE model. The errorbars correspond to 90% confidence range. Note that the PE results here incorporate precession and use Virgo data when available, unlike our search. We also perform PE separately with (2,2)-only aligned-spin waveforms and report the change in evidence when aligned-spin HM and precession effects are progressively included in PE.

Sr. No.	New candidate event	Bank	PE (90% credibility)					$\Delta \log_{10}(\text{evidence})$		ρ_{H}^2	ρ_{L}^2	IFAR (yr)		p_{astro}
			$m_1^{\text{src}} (M_{\odot})$	q	χ_{eff}	z	ρ_{network}^2	HM	HM+Prec.			per bank	overall	
1	GW190605.025957	13,0	130_{-50}^{+80}	$0.7_{-0.5}^{+0.3}$	$0.7_{-1.1}^{+0.3}$	$1.4_{-0.8}^{+0.8}$	84.4	-0.34	-0.4	43.0	46.5	11.4	0.59	0.88
2	GW190806.033721	8,1	60_{-20}^{+40}	$0.6_{-0.4}^{+0.3}$	$0.84_{-0.43}^{+0.15}$	$1.7_{-0.8}^{+1.0}$	59.2	-0.26	-0.28	35.8	33.8	4.6	0.46	0.86
3	GW190524.134109	10,0	60_{-20}^{+40}	$0.7_{-0.8}^{+0.3}$	$0.6_{-0.8}^{+0.3}$	$1.4_{-0.7}^{+0.8}$	67.4	-0.34	-0.34	23.3	44.4	3.6	0.43	0.85
4	GW191113.103541	9,0	90_{-40}^{+80}	$0.26_{-0.12}^{+0.46}$	$0.8_{-0.5}^{+0.2}$	$0.8_{-0.5}^{+0.8}$	90.0	0.24	0.28	36.4	39.1	1.8	0.21	0.76
5	GW190615.030234	10,0	70_{-20}^{+30}	$0.7_{-0.3}^{+0.3}$	$0.1_{-0.5}^{+0.4}$	$0.8_{-0.4}^{+0.5}$	92.4	-0.15	-0.14	24.1	50.5	1.5	0.20	0.75
6	GW190604.103812	12,0	130_{-50}^{+70}	$0.26_{-0.14}^{+0.33}$	$0.88_{-0.31}^{+0.11}$	$1.3_{-0.6}^{+0.9}$	57.0	0.74	0.9	29.6	38.1	1.3	0.13	0.68
7	GW191228.195619	14,0	300_{-120}^{+60}	$0.29_{-0.15}^{+0.24}$	$-0.2_{-0.5}^{+0.7}$	$0.38_{-0.15}^{+0.29}$	145.8	1.95	3.38	20.3	89.5	4.0	0.12	0.67
8	GW200304.172806	8,1	90_{-40}^{+70}	$0.5_{-0.4}^{+0.4}$	$0.88_{-0.51}^{+0.11}$	$1.2_{-0.7}^{+1.2}$	72.4	-0.09	-0.15	40.8	28.1	1.2	0.11	0.66
9	GW190530.030659	4,2	36_{-12}^{+27}	$0.5_{-0.3}^{+0.4}$	$0.5_{-0.3}^{+0.3}$	$0.6_{-0.2}^{+0.3}$	75.0	-0.1	-0.08	34.5	36.0	1.6	0.095	0.63
10	GW190511.163209	8,0	60_{-30}^{+120}	$0.3_{-0.2}^{+0.6}$	$0.88_{-1.41}^{+0.11}$	$1.7_{-1.1}^{+1.5}$	73.8	0.45	0.08	47.6	42.0	0.80	0.085	0.61
11	GW200210.100022	9,0	80_{-40}^{+30}	$0.23_{-0.10}^{+0.56}$	$0.93_{-0.38}^{+0.06}$	$1.4_{-0.6}^{+0.9}$	64.4	-0.39	-0.5	29.2	35.9	0.72	0.078	0.58
12	GW200301.211019	1,2	22_{-7}^{+35}	$0.6_{-0.5}^{+0.4}$	$-0.1_{-0.4}^{+0.7}$	$0.35_{-0.16}^{+0.24}$	72.2	-0.03	-0.16	36.5	38.3	2.5	0.070	0.56
13	GW190911.195101	12,0	80_{-30}^{+40}	$0.7_{-0.4}^{+0.3}$	$0.6_{-0.9}^{+0.3}$	$1.5_{-0.7}^{+0.8}$	65.0	-0.35	-0.31	25.3	55.4	0.60	0.061	0.54
14	GW190530.133833	12,0	90_{-30}^{+60}	$0.6_{-0.4}^{+0.4}$	$0.4_{-1.1}^{+0.5}$	$1.2_{-0.7}^{+1.0}$	56.4	-0.18	-0.11	38.2	31.7	0.58	0.058	0.53

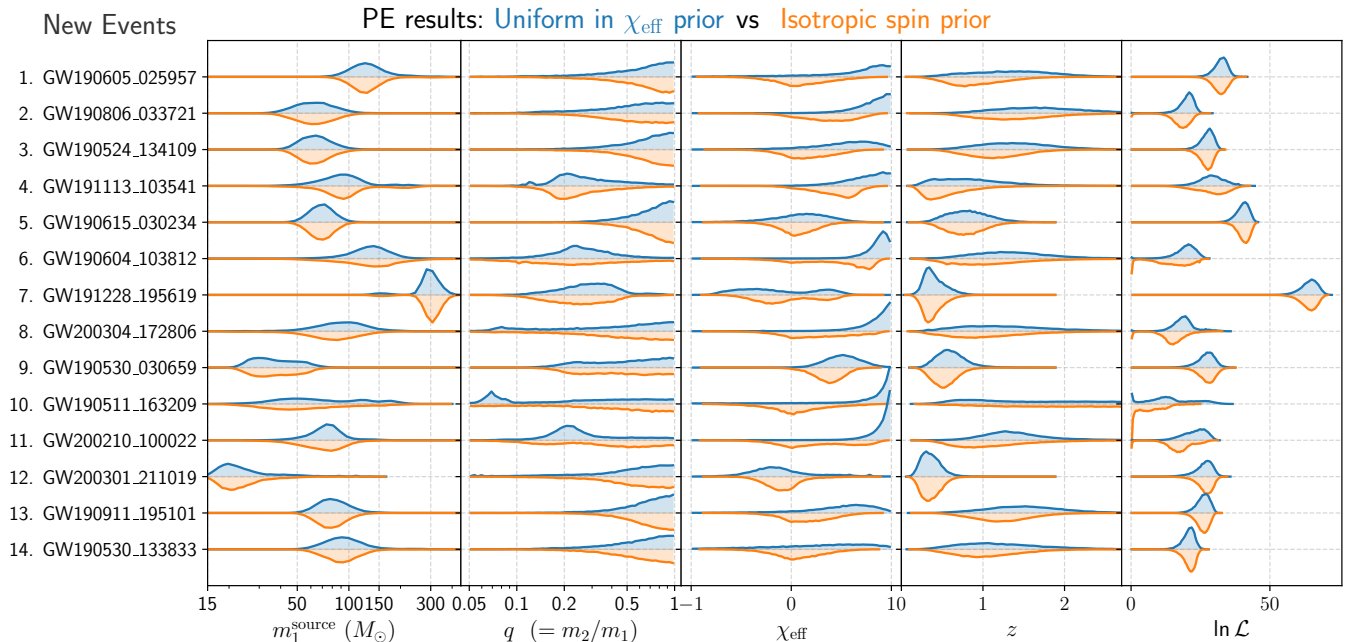


FIG. 3. Parameter estimation results for the new events under two different priors on BH spins. The largest difference between the two cases is when the posterior exhibits significant support for highly positive χ_{eff} under the uniform-in- χ_{eff} prior (blue). In such cases, the blue posteriors also have larger log-likelihood ($\ln \mathcal{L}$) values than orange (interestingly, in some of these cases, the blue posteriors have a larger support for high χ_{eff} and low q regions). More detailed corner plots from different runs are provided in Figs. 10 and 11, and comparison with the PE runs using IMRPhenomXPHM are in Fig. 9 in the Appendix.

TABLE II. Same as Table I but for candidate events with $p_{\text{astro}} > 0.5$ in our search which overlap with those first reported in the IAS (2, 2)-only searches: [10, 40]. The full comparison catalog is given in Table VI.

Event	Bank	PE (90% credibility)					$\Delta \log_{10}(\text{evidence})$		ρ_{H}^2	ρ_{L}^2	IFAR (yr)		p_{astro}
		$m_1^{\text{src}}(M_{\odot})$	q	χ_{eff}	z	ρ_{network}^2	HM	HM+Prec.			per bank	overall	
GW190711_030756	7, 1	60_{-20}^{+60}	$0.4_{-0.2}^{+0.4}$	$0.2_{-0.6}^{+0.6}$	$0.5_{-0.2}^{+0.5}$	101.4	1.07	0.82	32.5	68.9	290	38.7	0.99
GW190707_083226	7, 1	50_{-17}^{+21}	$0.7_{-0.4}^{+0.3}$	$0.0_{-0.6}^{+0.5}$	$0.8_{-0.4}^{+0.5}$	76.8	0.18	0.25	49.4	40.2	3.6	0.30	0.81
GW200109_195634	10, 0	60_{-20}^{+40}	$0.7_{-0.4}^{+0.3}$	$0.6_{-0.8}^{+0.3}$	$1.3_{-0.6}^{+0.9}$	79.8	0.05	0.15	42.6	36.2	1.8	0.23	0.78
GW190818_232544	8, 1	58_{-15}^{+29}	$0.7_{-0.4}^{+0.3}$	$0.77_{-0.35}^{+0.20}$	$1.3_{-0.6}^{+0.5}$	76.2	0.0	0.04	47.9	35.8	2.2	0.23	0.77
GW190906_054335	7, 1	38_{-17}^{+23}	$0.7_{-0.4}^{+0.3}$	$0.3_{-0.5}^{+0.4}$	$1.1_{-0.5}^{+1.1}$	61.4	0.03	0.23	27.3	43.6	0.92	0.064	0.55

TABLE III: Hanford–Livingston coincident events already reported in the GWTC-3 catalog [7] as detected by our pipeline and the 4-OGC catalog [14]. The inverse false alarm rate (IFAR) values in the GWTC-3 column are taken from the **GWOSC** catalog, which corresponds to whichever LVK pipeline achieved the highest astrophysical probability for that event in the GWTC-3 analysis. Note that we report our IFAR values after combining all our template banks (in contrast to some of the previous IAS searches where IFARs per bank were reported [8–10]). At the bottom of the table, we show the comparison with the 4-OGC events not in GWTC-3 catalog. We broadly recover the confident LVK detections, except some events which were vetoed or were below our collection threshold SNR ρ_{collect} (see section III C). Note however that the ρ_{collect}^2 value which we used is currently not a bottleneck for us and we plan to use a lower threshold value in future searches.

GWTC-3 events	Bank /comment	ρ_{H}^2	ρ_{L}^2	GWTC-3 ρ_{Network}^2	p_{astro}			IFAR (yr)		
					IAS	GWTC-3	4-OGC	IAS	GWTC-3	4-OGC
GW190403_051519	BBH_9	24.6	42.5	57.8	0.49	0.61	—	0.047	0.13	—
GW190408_181802	BBH_2	85.6	99.9	213.2	1.00	1.0	1.0	> 1000	> 1000	> 1000
GW190412_053044	BBH_3	79.2	245.1	392.0	1.00	1.0	1.0	> 1000	> 1000	> 1000
GW190413_052954	BBH_6	28.8	54.5	81.0	0.98	0.93	1.0	10.2	1.2	1.4
GW190413_134308	BBH_7	24.3	67.9	112.4	1.00	0.99	1.0	581	5.6	6.4
GW190421_213856	BBH_7	77.9	42.5	114.5	1.00	1.00	1.0	581	357	> 1000
GW190426_190642	Veto (BBH_12)	25.82	45.46	75.7	—	0.75	—	—	0.24	—
GW190503_185404	BBH_4	88.2	57.5	148.8	1.00	1.0	1.0	581	> 1000	> 1000
GW190512_180714	BBH_1	34.6	109.1	161.3	1.00	1.0	1.0	> 1000	> 1000	> 1000
GW190513_205428	BBH_4	91.7	57.6	156.2	1.00	1.00	1.0	> 1000	> 1000	> 1000
GW190514_065416	BBH_7	42.6	31.6	64.0	0.96	0.76	0.82	2.5	0.36	0.19
GW190517_055101	BBH_2	47.7	59.1	116.6	1.00	1.0	1.0	> 1000	> 1000	66.1
GW190519_153544	BBH_7	94.3	133.0	252.8	1.00	1.0	1.0	> 1000	> 1000	> 1000
GW190521_030229	Veto (BBH_16)	109.23	180.37	204.5	—	1.00	1.0	—	769	805
GW190521_074359	BBH_6	158.4	449.7	670.8	1.00	1.0	1.0	> 1000	> 1000	> 1000
GW190527_092055	BBH_6	27.4	53.9	64.0	0.97	0.85	0.94	4.1	4.3	0.37
GW190602_175927	BBH_9	46.5	112.1	174.2	1.00	1.0	1.0	581	> 1000	391
GW190701_203306	Veto (BBH_7)	34.87	55.9	125.4	—	1.00	1.0	—	175	0.13
GW190706_222641	BBH_8	93.6	72.9	179.6	1.00	1.0	1.0	> 1000	> 1000	> 1000
GW190707_093326	BBH_0	61.6	115.5	171.6	1.00	1.0	1.0	> 1000	> 1000	> 1000
GW190719_215514	BBH_8	32.3	45.0	62.4	0.83	0.92	0.92	0.35	1.6	0.25
GW190720_000836	BBH_0	46.9	58.2	118.8	1.00	1.0	1.0	581	> 1000	559
GW190725_174728	Veto (BBH_3)	27.35	55.99	82.8	—	0.96	0.96	—	2.2	0.41
GW190727_060333	BBH_6	74.3	67.9	136.9	1.00	1.0	1.0	> 1000	> 1000	> 1000
GW190728_064510	BBH_0	62.6	114.8	171.6	1.00	1.0	1.0	> 1000	> 1000	> 1000
GW190731_140936	BBH_6	31.7	43.6	77.4	0.97	0.83	0.92	4.7	3.0	0.43
GW190803_022701	BBH_6	34.7	52.9	86.5	0.97	0.97	1.0	5.6	13.7	2.4
GW190805_211137	BBH_6	22.8	53.2	65.6	0.99	0.95	—	12.9	1.6	—
GW190828_063405	BBH_4	115.6	147.0	272.2	1.00	1.0	1.0	> 1000	> 1000	> 1000
GW190828_065509	Veto (BBH_1)	50.14	56.48	104.0	—	1.00	1.0	—	> 1000	> 1000
GW190909_114149 ^a	BBH_7	41.4	36.0	81.9	0.64	0.15	—	0.10	0.038	—
GW190915_235702	BBH_4	92.4	77.1	171.6	1.00	1.0	1.0	> 1000	> 1000	> 1000
GW190916_200658	BBH_8	37.3	34.2	65.6	0.97	0.66	0.90	5.0	0.21	0.22
GW190917_114630	Below ρ_{collect}^2	—	—	68.9	—	0.77	—	—	1.5	—
GW190924_021846	BBH_0	35.9	103.9	144.0	1.00	1.0	1.0	581	> 1000	> 1000
GW190926_050336	BBH_6	48.7	36.4	65.6	0.94	0.54	0.92	1.6	0.91	0.27
GW190929_012149	BBH_9	43.2	75.1	94.1	0.94	0.87	0.99	1.6	6.2	3.1
GW190930_133541	Veto (BBH_1)	36.02	45.98	94.1	—	1.00	1.0	—	83.3	295
GW191103_012549	BBH_0	41.1	46.0	79.2	0.96	0.94	—	2.0	2.2	—
GW191105_143521	BBH_0	33.3	66.2	94.1	0.99	0.99	1.0	15.1	83.3	316
GW191109_010717	Veto (BBH_8)	82.74	164.37	299.3	—	0.99	1.0	—	> 1000	> 1000

^a GW190909_114149 is a marginal candidate in GWTC-3 which has $p_{\text{astro}} > 0.5$ from our pipeline.

GWTC-3 events	Bank /comment	ρ_H^2	ρ_L^2	GWTC-3 ρ_{Network}^2	p_{astro}			IFAR (yr)		
					IAS	GWTC-3	4-OGC	IAS	GWTC-3	4-OGC
GW191113.071753	Below ρ_{collect}^2	---	---	62.4	---	0.68	---	---	0.038	---
GW191126.115259	BBH_0	38.3	48.3	68.9	0.92	0.70	1.0	1.00	0.31	4.9
GW191127.050227	BBH_8	54.8	40.8	84.6	0.99	0.74	0.99	15.1	4.0	0.15
GW191129.134029	BBH_1	68.6	88.5	171.6	1.00	0.99	1.0	> 1000	> 1000	> 1000
GW191204.110529	BBH_2	32.5	65.6	77.4	0.99	0.74	0.99	14.3	0.30	1.6
GW191204.171526	BBH_0	95.6	185.1	306.2	1.00	0.99	1.0	> 1000	> 1000	> 1000
GW191215.223052	BBH_2	48.0	67.9	125.4	1.00	0.99	1.0	> 1000	> 1000	869
GW191222.033537	BBH_7	94.6	69.0	156.2	0.82	0.99	1.0	0.32	> 1000	> 1000
GW191230.180458	BBH_8	56.3	55.8	108.2	1.00	0.96	1.0	176	20.0	497
GW200128.022011	BBH_6	59.1	51.9	112.4	1.00	0.99	1.0	528	233	307
GW200129.065458	Veto (BBH_4)	203.73	342.75	718.2	---	0.99	1.0	---	> 1000	> 1000
GW200202.154313	BBH_1	24.2	88.3	116.6	0.99	0.99	1.0	8.0	> 1000	6.1
GW200208.130117	BBH_6	41.9	63.0	116.6	1.00	0.99	1.0	87.9	> 1000	917
GW200208.222617	BBH_8	32.4	37.3	54.8	0.11	0.70	---	0.007	0.21	---
GW200209.085452	BBH_4	64.3	37.0	92.2	0.96	0.97	0.99	2.1	21.7	1.1
GW200210.092254	Veto (BBH_3)	25.53	48.5	70.6	---	0.54	---	---	0.83	---
GW200216.220804	BBH_8	49.6	49.1	65.6	0.97	0.77	0.78	2.7	2.9	0.093
GW200219.094415	BBH_6	39.1	77.8	114.5	1.00	0.99	1.0	106	> 1000	22.9
GW200220.061928	Below ρ_{collect}^2	---	---	51.8	---	0.62	---	---	0.15	---
GW200220.124850	BBH_6	41.8	35.9	72.2	0.98	0.83	---	4.7	0.033	---
GW200224.222234	BBH_6	161.4	164.2	400.0	1.00	0.99	1.0	> 1000	> 1000	> 1000
GW200225.060421	BBH_1	76.6	48.1	156.2	1.00	0.99	1.0	> 1000	> 1000	> 1000
GW200306.093714	BBH_5	40.2	33.8	60.8	0.093	0.81	0.51	0.006	0.042	0.018
GW200308.173609	Below ρ_{collect}^2	---	---	50.4	---	0.86	---	---	0.42	---
GW200311.115853	BBH_4	156.2	108.4	316.8	1.00	0.99	1.0	> 1000	> 1000	817
GW200316.215756	BBH_1	29.2	62.2	106.1	1.00	0.99	1.0	106	> 1000	22.4
GW200322.091133	BBH_6	41.1	29.3	36.0	0.032	0.62	---	0.002	0.007	---
4-OGC events	Bank /comment	ρ_H^2	ρ_L^2	4-OGC ρ_{Network}^2	p_{astro}			IFAR (yr)		
					IAS	GWTC-3	4-OGC	IAS	GWTC-3	4-OGC
GW191224.043228	BBH_1	27.9	46.8	73.0	0.88	---	0.87	0.53	---	0.13
GW200106.134123	BBH_6	42.4	45.1	55.0	0.65	---	0.69	0.11	---	0.059
GW200129.114245	BBH_10	32.9	47.1	63.0	0.40	---	0.53	0.035	---	0.037
GW200210.005122	Below ρ_{collect}^2	---	---	70.0	---	---	0.74	---	---	0.042
GW200214.223306	BBH_8	37.5	32.4	55.0	0.69	---	0.72	0.13	---	0.079
GW200305.084739	Below ρ_{collect}^2	---	---	59.0	---	---	0.59	---	---	0.019
GW200318.191337	BBH_7	27.4	43.8	63.0	0.90	---	0.97	0.66	---	0.50

detector-frame masses, and we do not assume a separate prior over redshift z .

We drew $\sim 10^6$ samples according to this prior (each sample corresponding to the physical parameter set $[m_1, m_2, \chi_{1,z}, \chi_{2,z}]$), and assigned a weight to each sample based on its observable volume. As a proxy for the observable distance, we simply calculated the SNR for the sample at a fixed distance by simulating its waveform using `IMRPhenomXHM` and using the same reference PSD which was used to make the template banks (weight_{sample} \propto SNR³). Just for reference, for inspiral dominated waveforms, the observable volume roughly scales as $M_{\text{tot}}^{2.2}$ [42]. Using these samples, we then utilized the kernel density estimation method to construct probabilities for templates in our template banks (see appendix C of O22 for details on the density estimation method). Fig. 8 in the Appendix shows the cumulative probabilities for our banks, each of which is obtained by adding the weights of all the samples falling within the corresponding bank.

1. Comparison with astrophysical prior used in our (2, 2)-only banks

It is worth briefly comparing the astrophysical distributions we assumed here to those we assumed in our previous (2, 2)-only O3 searches. We split our banks roughly according to the detector-frame chirp mass $\mathcal{M}_{\text{chirp}}$ (the bank edges were uniform in $\log \mathcal{M}_{\text{chirp}}$) and further split each bank into subbanks based on the amplitude profiles of normalized (2, 2) waveforms [43]. We assumed that the total prior astrophysical probability within each of our banks was identical, and that the probability distribution within each bank was flat in the detector-frame component masses and also in the effective spin χ_{eff} (without taking the observable distance into account; we take this effect into account in the current search). Note that we also slightly increased our search space in this paper: previously, our banks were limited to $m_1^{\text{det}} \leq 200 M_{\odot}$ and $m_2^{\text{det}} \leq 100 M_{\odot}$ (see figure 2 of O22), while we now use

$$M_{\text{tot}}^{\text{det}} \leq 400 M_{\odot}.$$

III. RESULTS

A. New candidate events

Using our new search pipeline on the Hanford–Livingston data from the third observing run (O3), we find 14 candidate events with $p_{\text{astro}} > 0.5$ which have not been previously reported in the literature. We list the properties of these new candidates in Table I. In all tables in this paper, ρ_{H}^2 , ρ_{L}^2 columns correspond to incoherent SNR obtained from $|\rho_{22}|^2 + |\rho_{33}|^2 + |\rho_{44}|^2$ in the particular detector (note that we have orthogonalized the templates of different harmonics, so that they can be added in quadrature). The incoherent $\rho_{22}, \rho_{33}, \rho_{44}$ values may not correspond to those possible for a physical trigger. Thus, in some cases we see that $\rho_{\text{H}}^2 + \rho_{\text{L}}^2$ can even exceed the best-fit parameter estimation (PE) values ρ_{network}^2 . Further discussion of the PE runs are given below in Section III A 1, and we report 90% CL values of some of the binary parameters in Table I. We show the SNR contribution of individual modes separately in Table V in the Appendix.

We also mention the best bank_id, subbank_id for each event; the bank_id roughly increases with mass (see Fig. 8). Note that the high-mass banks in our case have much fewer templates than the low-mass banks (see Table I of [1]), which leads to considerable heterogeneity in the number of background triggers in the banks. Hence, the ρ^2 values needed for events to be above threshold can be different for different banks.

Other than running the pipeline on coincident triggers, we also artificially simulate background using 2000 timeslides (where we shift one of the detectors by unphysical amounts which are more than the light crossing time between the detectors) and run the pipeline on these in exactly the same way. This allows us to measure the inverse false alarm rate (IFAR) of our coincident triggers. We report this value within each bank and the overall IFAR after combining the background lists from all of our 17 banks. Additionally, for each trigger, the statistic p_{astro} is its probability of being of astrophysical origin; computing it involves estimating the astrophysical rate of events in addition to their IFARs. We estimate the p_{astro} values in a manner that is similar to that outlined in Appendix B of O22, from the distribution of foreground and background triggers according to

$$p_{\text{astro}}(\rho_{\text{rank}}^2) = \frac{\frac{dN}{d\rho^2}(\rho_{\text{rank}}^2 | \mathcal{S})}{\frac{dN}{d\rho^2}(\rho_{\text{rank}}^2 | \mathcal{S}) + \frac{dN}{d\rho^2}(\rho_{\text{rank}}^2 | \mathcal{N})} \quad (3)$$

where ρ_{rank}^2 in the above formula corresponds to our final ranking statistic value for the candidate events (see Ref. [2] for the full expression), and $dN/d(\rho_{\text{rank}}^2)$ corresponds to number density values from a 1D histogram

of the ranking statistic (which we separately calculate for the signal \mathcal{S} and background \mathcal{N} cases). Note that as the templates in our banks have astrophysical probabilities associated with them (see Section II D), and we use these values in calculating ρ_{rank}^2 . Hence, our IFAR and p_{astro} values are also dependent on our assumption of astrophysical distributions of binary parameters. We expect this dependence to be more significant for the ‘overall’ IFAR in comparison to the ‘per bank’ IFAR values quoted in Table I. We therefore separately provide the ‘per bank’ values in our table, so one can reweight them in a rough way for different astrophysical distributions than the ones assumed here.

1. Parameter estimation runs

We perform parameter estimation (PE) runs using the `cogwheel` package¹ [17] with the NAUTILUS sampler [44]. We use priors that are uniform in detector-frame constituent masses and comoving volume-time (VT) throughout this paper. Our fiducial prior for the BH spins is flat in effective spin χ_{eff} , but we also compare results with those obtained using an isotropic prior on individual spins (which is used for PE in the GWTC-3 and 4-OGC catalogs). Other extrinsic parameters have the standard geometric priors used in GWTC-3 [7]. We compute likelihoods using the relative binning/heterodyning method described in Ref. [45] as implemented in `cogwheel`. The relation between redshift and luminosity distance is based on the Planck15 cosmology [46]. Our fiducial parameter estimation runs are based on the IMRPhenomXODE waveform approximant [47] and include the effect of both HM and precession. Table I reports marginalized 1D posterior values for a relevant subset of parameters.

Other than the fiducial runs, we also perform two separate PE runs without precession, i.e., restricting to binaries with aligned spins: one run with a (2, 2)-only waveform approximant and the other with an approximant that includes HM as well. This helps us calculate the relative evidence (Bayes factor) due to including the effects of HM and HM + precession separately for the new candidate events; we show the logarithm of the Bayes factors in Table I. Four of the new candidate events (the ones numbered 4, 6, 7, 10) have Bayes factors larger than unity for HM, and the detection of these candidates likely benefited the most from our search containing HM. Most of the remaining events have Bayes factors for HM that are lower than unity, and we judge that the detection of these additional candidates was a result of just an overall improvement of our search’s sensitivity in the high mass/redshift region due to e.g., improved template coverage and background estimation.

¹ <https://github.com/jroulet/cogwheel>

We show a few select 2D posteriors of our new candidate events in colored contours in Figs. 1, 2 and 7. We also overplot the contours from events in GWTC-3, 4-OGC and the IAS (2,2)-only O3 catalogs in light gray. Our search only covers events with Hanford–Livingston coincidence triggers, but we include all binary BH events that are part of the LVK catalogs through O1–O3 in these figures. Note that the posteriors are bi-modal for some events, which show up as two contours in the plot.

We add dashed lines to mark the approximate limits of sensitivity in the top panel of Fig. 1. The dashed line in the top-right of the panel marks the region where the binary starts moving out of band (we take this to happen when the detector frame mass equals $400 M_{\odot}$, which is the limit of our template bank). The dashed line in the top-left marks the contour of constant detector-frame luminosity for an inspiral-dominated equal-mass binary; it roughly delineates the parameter limits past which binaries are too faint to be observable. It is also worth mentioning that the size of the contours increases for higher masses as the number of cycles in band starts to decrease. In the inspiral phase, the chirp mass is well-measured, but this no longer continues to be the case for high-mass events where the SNR is dominated by the merger and ringdown phase and the total mass of the binary starts to be measured better.

We show the marginalized 1D posteriors for our new candidate events under the aforementioned two different spin priors in Fig. 3. Figs. 10 and 11 in the Appendix show full corner plots from different PE runs. Some of the events in Fig. 3 (e.g., the ones numbered 2, 6, 8, 10, 11) have posteriors that show significant support for large, positive effective spin χ_{eff} under the uniform in χ_{eff} prior. The isotropic spin prior recovers a lower likelihood for these events, since the prior pulls the sampler away from the high χ_{eff} solution.

GW191228.195619 has the largest evidence for HM (~ 90) and also for the combination of HM+precession (~ 2400). We show a corner plot corresponding to this event in Fig. 4 for our three PE runs, and we indeed see significant support for both HM and precession. Note that for the (2,2) (green) and (2,2) + HM (orange) cases, the distribution of the primary component’s in-plane spin component $\chi_{1,\perp} = \sqrt{\chi_{1,x}^2 + \chi_{2,y}^2}$ is that of its prior conditioned on the other parameters. For these cases, we set the in-plane spin components to zero when evaluating likelihoods. Within 90% CL, we find $\chi_{1,\perp}$ to be $0.57^{+0.20}_{-0.25}$. Note also that the total SNR^2 (~ 110) recovered by our non-precessing Hanford+Livingston search is significantly smaller than $\rho_{\text{network}}^2 \sim 146$ obtained from a PE run which includes both the effects of orbital precession and data from the Virgo detector. Therefore, we conjecture that the significance of this event could be improved in future searches that include the effects of precession and/or Virgo data.

We also compare our results against PE runs using the IMRPhenomXPHM approximant [48] (under the two differ-

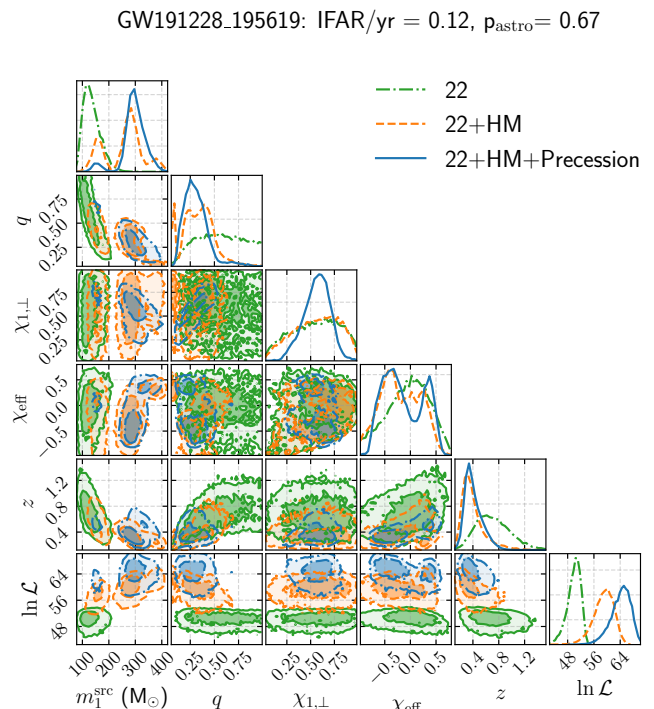


FIG. 4. A closer look at one of the most interesting candidate events from our search: GW191228.195619. We perform the PE runs in the three cases labelled above and find significant support not just for HM, but also for precession. This could be one of the reasons why our search (which includes HM) was able to recover this candidate (we also think a future search that incorporates precession can likely further improve the significance of this event). Other interesting properties of this candidate are as follows. It is, by far, the highest mass merger candidate ($M_{\text{tot}}^{\text{src}} = 380^{+70}_{-110} M_{\odot}$) detected with $p_{\text{astro}} > 0.5$ in gravitational wave data until now. The mass posterior for its secondary BH ($m_2^{\text{src}} = 90^{+40}_{-40} M_{\odot}$) overlaps with the upper mass-gap. Its mass ratio is bounded away from unity ($q = 0.29^{+0.24}_{-0.15}$). It also has significant support for the in-plane primary spin $\chi_{1,\perp}$ to be non-zero (for the two non-precessing cases, the posterior of $\chi_{1,\perp}$ is the same as its conditional prior).

ent MSA [49] and NNLO [50] prescriptions for evolving the spins) in Fig. 9 in the Appendix; we find good agreement in most of the cases. It would be interesting to compare the PE for these events with NR surrogate models (e.g. [51]) in the future.

We will discuss interesting astrophysical properties of our new candidate events in Section IV below.

B. Comparison to the IAS (2,2)-only catalogs

In Table II, we report the candidate events with $p_{\text{astro}} > 0.5$ from our pipeline which have already been reported in the previous (2,2)-only IAS searches in the O3 data [10, 40]. The full comparison catalog including lower p_{astro} candidates is given in Table VI. Overall, we

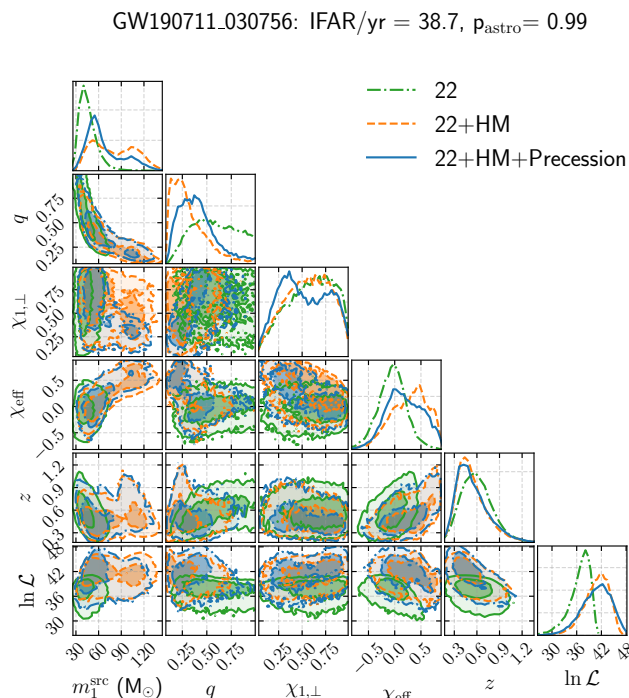


FIG. 5. GW190711.030756 is among the most significant candidates recovered in our search. It was first reported in our previous IAS (2, 2)-only search O22, however, its IFAR in our HM search is comparatively much larger (i.e., 38.7yr instead of ~ 2 yr). Our search also recovers an additional 10 points in the total SNR^2 compared to the (2, 2)-only search. Indeed, we also see a significant evidence for higher modes in the PE results. The mass ratio (q) posterior has its median at 0.37, but also has a small tail towards equal masses. Its total mass ($= 90_{-30}^{+50} M_{\odot}$) lies within the upper mass gap.

recover 6 events with $p_{\text{astro}} \geq 0.5$.

We caution against directly comparing the sensitivities of the (2, 2)-only and (2, 2) + HM pipelines from Table VI as there are multiple differences: (i) including HM in the search, (ii) using a different astrophysical prior (see Section IID) (iii) additional glitch cleaning at high masses (see Section IC). It is worth mentioning though that we recover the events which were reported in previous IAS catalogs with $p_{\text{astro}} > 0.6$, except GW190704.104834 (this event was in BBH-0 in O22 and we checked that the difference in the astrophysical priors between the pipelines was large for that bank). We collect a larger number of triggers in the HM search as compared to a (2, 2)-only search, so we raised the collection threshold to mitigate the increased memory requirements. This caused us to miss low-SNR events that were reported by (2, 2)-only pipelines with lower collection thresholds in the previous literature. We further discuss this point in Section III C 2 below.

One notable event in Table II is GW190711.030756. The IFAR of this event in our HM search is 38.7yr as opposed to ~ 2 yr in the (2, 2)-only search O22 (after accounting for the trials factor in O22 due to the number

of banks searched). We show a corner plot for this event in Fig. 5. Indeed, GW190711.030756 also shows a significant evidence for higher modes and our search recovers an additional 10 points in SNR^2 compared to the (2, 2)-only search. See Fig. 3 and section III A.2 of O22 for a detailed discussion of the properties of this event.

C. Comparison to the LVK and OGC (2, 2)-only catalogs

In Table III, we compare our pipeline’s results for the O3 Hanford–Livingston coincident events published in the GWTC-3 catalog² [7]. The GWTC-3 catalog combines results from four pipelines: three that search using templates which only contain the (2, 2) mode: GstLAL, Multi-Band Template Analysis (MBTA) and PyCBC [52–54]; and one that searches for transient signals with minimal assumptions about sources, cWB [55]. We also include the comparison with the 4-OGC catalog taken from the summary data in the repository³ listed in [14]. Note that the quoted GWTC-3 squared SNR, ρ_{Network}^2 , is from LVK’s PE runs for the events. The search SNR^2 is generally lower, and varies between the different pipelines that the LVK uses.

We broadly recover the confident LVK detections, except some vetoed/missed events which are discussed in more detail in the subsections below. Overall, 9 events GWTC-3 events in Table I were vetoed in our pipeline. 4 GWTC-3 events fell below our trigger collection SNR threshold (GW190917.114630, GW191113.071753, GW200220.061928, GW200308.173609), note that these were confidently detected by only one of the LVK pipelines. Three GWTC-3 events were detected with $p_{\text{astro}} < 0.5$ in our pipeline (GW200208.222617, GW200306.093714, GW200322.091133), note again that these were confidently detected by only one of the LVK pipelines.

At the end of Table III, we include comparison with the list of 7 events in 4-OGC which are not present in GWTC-3 catalog (from which we recover 4 with $p_{\text{astro}} > 0.5$ and 2 were below our collection SNR threshold). GW190909.114149 is a marginal candidate in GWTC-3 which has $p_{\text{astro}} > 0.5$ from our pipeline. We still include it in Table III as it was first a significant candidate in GWTC-2 [5], but later updated to be in the marginal list [6]. We also checked the overlap of our new candidate event list with the sub-threshold candidate list (i.e., which have $p_{\text{astro}} < 0.5$ but $\text{FAR} < 2 \text{ day}^{-1}$) released by the LVK collaboration: GWTC-2.1 and GWTC-3 [6, 7]; we show the corresponding comparison in Table V in the Appendix. In the same table, we also show the overlap

² <https://gwosc.org/GWTC-3/>

³ https://github.com/gwastro/4-ogc/blob/master/search/4OGC_top.txt

of our new candidate list with sub-threshold candidates from the IAS (2,2)-only pipeline [10, 40].

1. Vetoed events

Our pipeline includes a series of signal consistency checks in order to veto triggers that are likely to arise from noise transients (glitches) to improve our search sensitivity (see section I of [8]). The vetoes are designed in a way that they are falsely triggered by real signals with only a low probability (a few percent) if their waveforms are accurately modeled by templates in the bank, and the noise is Gaussian. If a loud signal displays effects which are not present in our templates, like precession or eccentricity, the chances of the veto mis-identifying it as a glitch can be much higher. GW190521.030229, GW191109.010717 and GW200129.065458 were reported to be fairly high SNR with imprints of precession [7, 56], which could be the reason for them being vetoed. For example, the presence of higher modes in GW190521 is disfavored with a Bayes factor of $10^{-0.38}$, while a precessing signal is favored with a factor of ~ 10 [56].

GW190701.203306 was vetoed due to excess power present after subtracting the best-fit waveform (note that the data around this event was treated for scattered light glitches [5]). Out of the ~ 40 veto tests that we apply to events, we noticed GW190828.065509 and GW190930.133541 each failed just one test (namely, the split test with chunk sets, and the χ^2 test with 20 chunks, respectively).

We noticed a small issue in the pipeline where we artificially veto triggers very close (~ 50 s) to the edge of the timeseries files; this led to the event GW190725.174728 being vetoed. We will fix this issue in future searches. The event GW190426.190642 was detected confidently by only one of the LVK search pipelines and got vetoed in our case.

We expect to recover some of loud vetoed events if we also include precession in our template banks. Alternatively, one could formulate a procedure to override vetos or changing their thresholds based on injections with precessing waveforms. We leave exploring these directions to future work.

2. Other missed/downweighted events

As we discussed earlier in Section II B, we set a particular SNR threshold (ρ_{collect}) to collect triggers from individual detectors. We do this in order to regulate the number of single-detector triggers that are passed to the more costly coincidence step of the pipeline. If we set the threshold based on the quadrature sum of the SNRs of the (orthogonalized) harmonics, we collect more triggers in a HM search as compared to a (2,2)-only search with the same threshold. Hence, we raised the collection

threshold ρ_{collect} (see Section II B 1 for a detailed discussion). Due to this, we missed low-SNR events that were reported by (2,2)-only pipelines in the previous literature. We label the events which fell below this threshold as “Below ρ_{collect}^2 ” in the table, where the threshold ρ_{collect}^2 depends on the number of templates in the bank and is therefore different for different banks. On further investigation, using a smaller value of ρ_{collect}^2 is feasible with our current search setup, and thus we plan to lower the threshold in future searches.

We do not include the following events in Table III because they were detected in Livingston–Virgo or Hanford–Virgo coincidence, or single detector search, all of which we have yet to run: GW190620.030421, GW190630.185205, GW190708.232457, GW190814, GW190910.112807, and GW190925.232845. We also only searched for BBH mergers in this paper, and did not recover the NSBH candidates GW191219.163120 and GW200115.042309 (in addition, the posterior probability for GW200210.092254 peaks in the NSBH region [7] and thus it was vetoed in our search). We hope to perform coincident searches which would also include Virgo (and KAGRA) in the future. We also intend to perform a separate search for NSBH mergers including our HM pipeline in a future paper.

GW191222.033537 was detected with $p_{\text{astro}} > 0.5$ in our pipeline but has comparatively a much higher false alarm rate. We checked that it was downweighted due to being in the proximity of a glitch (which led to the event acquiring unphysical amounts of SNR in HM).

IV. INTERESTING ASTROPHYSICAL PROPERTIES OF THE NEW CANDIDATE EVENTS

In this section, we discuss interesting astrophysical properties of the 14 new candidate events, whose parameters we have reported in Table I and in Figs. 1, 2 and 3.

A. Masses in the IMBH range and pair instability mass gap

Black holes roughly within the mass range 10^2 – $10^5 M_{\odot}$ are designated as intermediate-mass black holes (IMBHs). Several IMBH candidates have been suggested by electromagnetic observations, but these lack conclusive confirmation [57]. Gravitational waves have the potential to definitively detect objects in this regime, e.g., [56, 58]. In our search, at $> 95\%$ credibility, 4 candidate events have total masses in the IMBH range (GW190605.025957, GW190604.103812, GW191228.195619 and GW190530.133833). Among them, GW191228.195619 has the highest total mass (and also has the highest primary mass $300_{+60}^{-120} M_{\odot}$), which makes it, by a large margin, the most massive candidate

with $p_{\text{astro}} > 0.5$ detected in gravitational wave data so far.

Another interesting regime in BH masses is the pair instability mass gap. This is the regime in which stars undergo pair-instability supernova (where they are completely disrupted and no remnant is left behind). Otherwise, the stars undergo pulsational pair-instability supernova and iteratively lose their mass before collapsing to a black hole. These processes are expected to produce a gap roughly between $65\text{--}135 M_{\odot}$ in the distribution of BH mass. Note however that the exact boundaries of such a gap are not well determined, as they depend on multiple uncertain factors such as the rate of carbon to oxygen burning in the core $^{12}\text{C}(\alpha, \gamma)^{16}\text{O}$, angular momentum transport, metallicity, wind loss, etc. [59–62].

Recent analyses have not found any conclusive evidence for the upper mass gap in the observed BH mass distribution, e.g., [63, 64]. This either challenges the current theoretical models of stellar evolution, or the gap might be filled by black holes formed via alternative mechanisms such as hierarchical mergers [65–68], or from the gaseous disk channel [69, 70]. In our search, at 90% CL, 9 candidates have median mass of the primary BH lying between $65\text{--}135 M_{\odot}$ (# 1, 4, 5, 6, 8, 10, 11, 13, 14 in Table I). One of our candidates: GW191228_195619 has its secondary BH mass 90_{-40}^{+40} overlapping with the mass-gap range. Our new candidate events could be helpful in estimating the abundance of BH (or rate of BH mergers) in/beyond the pair-instability mass regime. This can also shed light on BH progenitor channels.

B. High redshifts

In our search, we find that 9 of our new candidates have redshift $z > 0.5$ at $> 95\%$ CL (# 1, 2, 3, 6, 8, 10, 11, 13, 14 in Table I). Finding high-redshift BHs can be important to answer questions such as: How does the merger rate of BHs evolve with redshift [71]? Does the merger rate change in a different manner compared to the the star formation rate (which peaks at $z \sim 2$ [72])? Furthermore, different BH formation channels can have different predictions for the merger rate at high redshift [73, 74]. For example, the chemically homogeneous evolution channel produces BBHs of relatively higher masses and lower redshifts than the common envelope evolution channel [75]. In the dynamical channel, massive BHs can have relatively longer delay times compared to star formation [76]. The redshifts of binaries can be also be correlated with other properties of BHs, e.g., spins [77–79]. We aim to test some of these models in a future population inference study.

C. Preference for positive effective spins

Measuring spins of the black holes is one of the best ways to distinguish between isolated and dynamical for-

mation channels. In the isolated channel, accretion can lead to spins of BHs which are aligned in the direction of the binary angular momentum (leading to positive values of the effective spin parameter χ_{eff}). Dynamical channels, on the other hand, predict the astrophysical χ_{eff} distribution to be symmetric around 0. This is because the spins BH captured into a binary are not expected to be preferentially aligned along any particular direction. From the PE runs under our fiducial prior, 6 candidates have effective spin $\chi_{\text{eff}} > 0$ at $> 95\%$ credibility (# 2, 4, 6, 8, 9, 11 in Table I). Note however that χ_{eff} posteriors are significantly dependent on the prior as seen in the comparison in Fig. 3. Though, even under the isotropic spin prior, some of the new candidate events still have mild preference for $\chi_{\text{eff}} > 0$.

Note that the preference for $\chi_{\text{eff}} > 0$ in our detection catalog does not immediately mean that astrophysics prefers this scenario, as this could be caused by selection effects. One of the selection effects is that positive χ_{eff} binaries are louder than their negative counterparts; due to the orbital hangup effect, the positive χ_{eff} binaries merge later and have power at higher frequencies [80, 81]. This effect is much more prominent for high mass binaries (where a significant portion of signal is masked by the low frequency end of the PSD) as we show in Fig. 6. There is another effect which further downweights high-mass negative χ_{eff} signals. Their waveforms have a short duration in band and therefore can be more effectively mimicked by glitches. This degrades the sensitivity to such systems in our search [2] when we perform the background dependent reweighting in our ranking statistic (see Section II C 3 and Ref. [2]). To robustly determine if the true astrophysical distribution also favors $\chi_{\text{eff}} > 0$ at high masses, we plan to do a population study (where we will use injections with both positive and negative χ_{eff} values to determine our pipeline selection function).

D. Asymmetric mass ratio systems

Five of our new candidates have median mass ratio $q < 0.5$ (# 4, 6, 7, 10, 11 in Table I). Finding sources with asymmetric mass ratios can shed light on the formation channels [23]. The globular cluster (dynamical) channel predicts that most merging BBHs have nearly equal masses [82]. This is because higher mass BHs in a globular cluster sink to their cores due to dynamical friction and vice versa for lighter BHs. The caveat is that if clusters can retain merger products, they can produce “second-generation” mergers whose mass ratios can deviate significantly from unity [83]. In the isolated binary channel, in certain cases, an initially asymmetric mass ratio system can evolve toward a more symmetric configuration due to mass accretion episodes [84, 85]; note that the reverse scenario has been proposed as well (see e.g., Ref. [86]). Another interesting property of asymmetric mass ratio and high total mass systems is that subdominant ringdown modes have a higher chance of

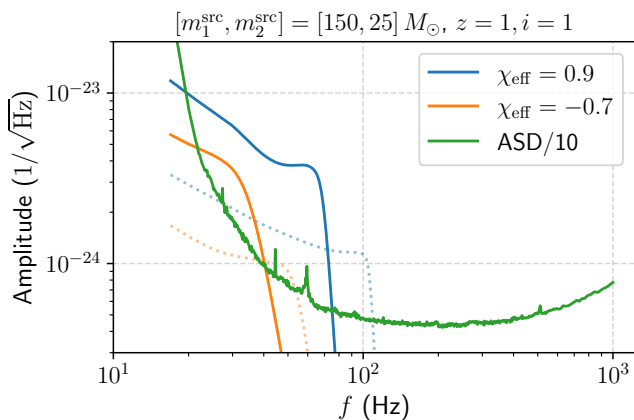


FIG. 6. Amplitude distribution of GW signal for a particular high-mass binary in the positive (negative) χ_{eff} case in shown in blue (orange). We also show the typical detector noise distribution curve which is labelled as ASD (amplitude spectral density). High-mass binaries have mergers at low frequencies. For such cases, the SNR of the binary can be significantly different depending on its χ_{eff} value, and this can lead to a large selection bias for $\chi_{\text{eff}} > 0$ in the high-mass detection catalog. The solid blue and orange lines correspond to the (2, 2) mode, and the dotted lines to the (3, 3) mode.

being observable in such systems, see e.g. [28].

V. DISCUSSION

A. Dependence on the choice of astrophysical prior

Our estimate of p_{astro} and our overall IFAR depend on the astrophysical prior used in the search, and that dependence is strongest in the case of near-threshold detections like some of the new candidates in our catalog list in Table I.

To facilitate further analysis and comparisons between different astrophysical priors, we make our posterior samples and other relevant information public at https://github.com/JayWadekar/GW_higher_harmonics_search. These can be used to reweight our results with other choices of priors (see e.g., [87]). The biggest difference in our astrophysical prior choice compared to other catalogs [7, 14] is for the BH spins. We use a prior that is flat in the effective spin parameter χ_{eff} . One motivation lies in the fact that χ_{eff} is often the best-measured spin parameter, and hence we want to give equal weights to all physically possible values of that parameter [88]. On the other hand, using an isotropic spin prior will significantly down-weight large (positive or negative) effective spins and can make it harder to reweight the results to a different prior. We also provide PE samples for posteriors sampled under the isotropic spin prior in the above repository. Another difference in our priors is for the case of total mass and mass ratios.

It is also worth discussing how our other priors compare with the results of Abbott *et al.* [63]. We used a search prior uniform in $\log q$, whereas, Ref. [63] modeled the distribution as a power law q^β and found $\beta = 1.1^{+1.7}_{-1.3}$. We used a simple power law prior for the detector frame total masses $P(M_{\text{tot}}^{\text{det}}) \propto M_{\text{tot}}^{-2}$ and did not include any separate prior over redshift. Ref. [63] modeled the source primary mass distribution as a power law m_1^α with $\alpha = 3.5^{+0.6}_{-0.56}$ supplemented by a Gaussian peak at $34^{+2.6}_{-4.0} M_\odot$. Ref. [63] modeled the merger rate as $(1+z)^\kappa$ and found $\kappa = 2.9^{+1.7}_{-1.8}$. The motivation for our prior choices was again to make it easy to reweight our results (both p_{astro} and overall IFAR values) later in a hierarchical population analysis (especially for the high mass and low mass ratio parameter space), see e.g., [89].

A full population analysis not only requires the PE samples but also the p_{astro} of each event [89]. For this reason, we also provide a file, `IAS_HM_03_triggers.hdf`, in the repository that contains the full list of triggers (including the sub-threshold ones). Just for reference, we report subthreshold events ($0.1 < p_{\text{astro}} < 0.5$) in Table VII in the Appendix.

B. What is the gain/loss in sensitivity due to including HM in the search?

Unfortunately, we cannot currently answer the above question by comparing the results from our search to those from the previous IAS (2, 2)-only searches [10, 40]. This is because our search not only includes the effect of HM, but also includes the improvements (for all modes) due to downweighting noise transients (see Section II C and [2]). Furthermore, compared to earlier, we use a different astrophysical prior (see section IID) and use a different waveform approximant for modeling the (2, 2) waveforms (IMRPhenomXAS [41] instead of IMRPhenomD [90]). For us to isolate the effect of HM, we will need to rerun our search (ideally on injections) with all the settings to be the same except having only (2, 2) modes in the template banks. We leave this study to a future work.

Previous studies have noted that the larger variety in waveform morphologies (brought by the inclusion of higher modes) can lead to a loss of sensitivity in the search, as the number of background triggers is increased, see e.g., [32, 35]. This can be understood from the fact that, with higher modes, the shape of the waveform also depends on the inclination and orbital phase, and these additional degrees of freedom increase the trials factor when finding the best-matching template. In our search, we do not blankly add additional degrees of freedom to the templates throughout the parameter space. Instead, our new detection statistic (see Section II B and [2]) includes HM while simultaneously marginalizing the likelihood over the extrinsic parameters (which are the same as in the (2, 2)-only search). This marginalization naturally downweights fine-tuned solutions, approaching

the optimal statistic and preventing an undue increase of the trials factor (e.g., the edge-on solutions get naturally downweighted when we marginalize over distance, as their observable volume is smaller).

In our ranking statistic for the triggers, we also marginalize over the ratios of the SNR amplitudes of HM: $|\rho_{33}/\rho_{22}|$ and $|\rho_{44}/\rho_{22}|$. In this integral, we use a prior distribution for $|\rho_{ii}/\rho_{22}|$ derived from our astrophysical prior. Note that the prior on $|\rho_{ii}/\rho_{22}|$ can be very different for templates in different regions of parameter space. For example, the median of our prior for $|\rho_{33}/\rho_{22}|$ is 0.04 for Bank 0 (a low-mass bank), while it is 0.3 for Bank 14 (a high-mass bank). If we did not include such a prior, we would indeed expect to encounter a large loss of sensitivity on including HM. Comparing the performance of our search on events detected in previous (2, 2)-only catalogs (see Tables III and VI), we can confirm that our search sensitivity for these events has not been significantly degraded and is roughly comparable.

We also find that in our new search, the significance of a few previously reported marginal events is increased significantly (GW190711_030756, GW200216_220804). Especially for the case of GW190711_030756, we suspect that the increase in sensitivity is due to addition of HM, but to test this we plan to do an injection study in the future.

The downside of using a prior distribution on $|\rho_{ii}/\rho_{22}|$ is that it is dependent on our choice of astrophysical prior (which is currently not precisely known). Especially, the mass ratio distribution is not very well constrained and affects our prior for $|\rho_{ii}/\rho_{22}|$. Using a different distribution for q than the true astrophysical distribution can indeed lead to some loss of sensitivity. We chose a broad prior (flat in $\log q$) in our search, with the motivation that such a prior can be easily reweighted later in a hierarchical population analysis.

Even though including HM can cause some loss in sensitivity for near-threshold equal mass systems, note that detecting even a few events with asymmetric-mass ratios can inform our population estimates much more than detecting a slightly larger number of equal-mass systems. It is worth drawing an analogy here to the case of spin distribution of templates used in (2, 2)-only searches. Neglecting templates with negative χ_{eff} indeed improves the search sensitivity to near-threshold $\chi_{\text{eff}} \gtrsim 0$ systems, but finding even a few $\chi_{\text{eff}} < 0$ systems can greatly help us distinguish between progenitor channels of BHs. We thus argue the goal of a search should not solely be to maximize the total number of detections, but to holistically cover most of the interesting regions of the binary parameter space. A similar argument also holds for a precessing search, where detecting even a few events with significantly misaligned spins can shed more light on the formation channels of binaries as compared to detecting a larger number of near-threshold aligned/zero spin mergers.

VI. CONCLUSIONS

Nearly all gravitational searches performed till now only include the quadrupole mode of the full GW waveform predicted by general relativity. In our companion papers Wadekar *et al.* [1, 2], we develop new efficient methods to introduce higher-order modes (HM) in our search pipeline (section II). This helped us perform the first search over the full binary black hole parameter space (i.e., over all binary inclinations) with including HM in our templates. Compared to our previous pipeline, we introduced additional improvements to remove/downweight noise transients (especially at low frequencies), which further improved our sensitivity to high mass and high redshift systems (section II C).

We searched over public data from the third LIGO–Virgo observing run and found 14 new candidate events with $p_{\text{astro}} > 0.5$ (see Table I and section III). Some of the new candidate events have several interesting astrophysical properties (section IV) such as: (i) masses in the IMBH range and pair instability mass gap, (ii) high redshifts, (iii) preference for positive effective spins, (iv) asymmetric mass ratios.

By simply summing over the complements of p_{astro} values of our new candidate events from Table I, we expect that roughly 4 of the 14 new events are noise transients instead of being astrophysical signals. However, we note that estimates of p_{astro} and source parameters depend on the choice of prior, and we discuss this dependence in section V⁴.

We also compared our pipeline’s results for the events published in previous IAS catalogs (Tables II & VI), and in the GWTC-3 and 4-OGC catalogs (Table III). We broadly recovered the high-significance events, except some events which were either vetoed by our pipeline or fell below our trigger collection SNR threshold, which we discuss in detail in section III C (we also mention some possible future improvements in this regard).

Our methodology for efficiently including realistic effects like HM in GW templates will continue to be useful for high-precision searches in upcoming and future gravitational wave experiments [91–96]. One particular example in which HM will be especially useful is when searching for extreme-mass-ratio inspirals in LISA [97, 98].

A. Future work

We plan to inject simulated gravitational-wave signals in the data and compare the fraction of injections recovered by our pipeline. The injections will help us determine the gain/loss in volume-time sensitivity in different

⁴ We provide our posterior samples at https://github.com/JayWadekar/GW_higher_harmonics_search, which can be used to reweight our results for a different astrophysical prior.

regions of the parameter space due to including HM in our search. The injections will also help us gauge the level of improvement due to the additional glitch treatment methods that we described in section **II C**. We plan to use the injection parameters from Abbott *et al.* [7], which will help us perform an apples-to-apples comparison of our sensitivity with other pipelines. Having injections will also help quantify the selection function of our current pipeline and help in population inference studies. The new events reported here have moderate IFARs (the best event has $\text{IFAR} \sim 0.6 \text{ yr}$), thus a methodology to combine confident and marginal events in population inference will be required [89]. We expect our sensitivity to be higher than other searches for asymmetric mass ratio events due to addition of HM. Our sensitivity could also be higher for high-mass and high-redshift regions due to using improved glitch treatment methods and adding HM. Note that, in certain regions of the parameter space, having higher sensitivity can improve population estimates even if we have null/marginal detections. We note some interesting population inference questions in section **IV**.

Currently, nearly all searches also ignore the effects of precession or eccentricity in their waveforms. Some of the challenges for including these effects are similar to the ones for HM: significant increase in the template bank size and loss of sensitivity due to collecting additional background. We hope to develop methods similar to the ones implemented in our search to help tackle those searches in the future.

ACKNOWLEDGMENTS

We thank Horng Sheng Chia, Ajith Parameswaran, Will Farr, Vishal Baibhav, Katerina Chatziioannou, Vicky Kalogera, Sylvia Biscoveanu, Amanda Farah, Daniel Holz, Salvatore Vitale, Tom Edwards, Zoehyr Doctor, Suvodip Mukherjee and Mukesh Singh for helpful discussions. DW gratefully acknowledges support from the Friends of the Institute for Advanced Study Membership and the Keck foundation. TV acknowledges support from NSF grants 2012086 and 2309360, the Alfred P. Sloan Foundation through grant number FG-2023-20470, the BSF through award number 2022136, and the Hellman Family Faculty Fellowship. MZ is supported by NSF 2209991 and NSF-BSF 2207583. BZ is supported by the Israel Science Foundation, NSF-BSF and by a research grant from the Willner Family Leadership Institute for the Weizmann Institute of Science. This research was also supported in part by the National Science Foundation under Grant No. NSF PHY-1748958. We also thank ICTS-TIFR for their hospitality during the completion of a part of this work.

This research has made use of data, software and/or web tools obtained from the Gravitational Wave Open Science Center (<https://www.gw-openscience.org/>), a service of LIGO Laboratory, the LIGO Scientific Col-

laboration and the Virgo Collaboration. LIGO Laboratory and Advanced LIGO are funded by the United States National Science Foundation (NSF) as well as the Science and Technology Facilities Council (STFC) of the United Kingdom, the Max-Planck-Society (MPS), and the State of Niedersachsen/Germany for support of the construction of Advanced LIGO and construction and operation of the GEO600 detector. Additional support for Advanced LIGO was provided by the Australian Research Council. Virgo is funded, through the European Gravitational Observatory (EGO), by the French Centre National de Recherche Scientifique (CNRS), the Italian Istituto Nazionale di Fisica Nucleare (INFN) and the Dutch Nikhef, with contributions by institutions from Belgium, Germany, Greece, Hungary, Ireland, Japan, Monaco, Poland, Portugal, Spain.

Appendix A: Additional plots and tables

TABLE V. We show the SNR^2 contribution from the different harmonics for the new candidate events in our search (we sum over the Hanford and Livingston contributions in this table). We also cross-check our list with the sub-threshold candidates given in GWTC-3 [7] and the IAS (2, 2)-only catalogs [10, 40]; we report properties of the sub-threshold candidates which have GPS times differing by less than a second. It is worth noting that the 5 overlapping candidates in GWTC-3 were all from the PyCBC-BBH (pycbc_highmass) pipeline.

Sr. No.	New candidate event	This search			GWTC-3 sub-threshold			IAS 22-only sub-threshold		
		ρ_{22}^2	ρ_{33}^2	ρ_{44}^2	ρ_{22}^2	IFAR	p_{astro}	ρ_{22}^2	IFAR	p_{astro}
1	GW190605_025957	75.7	10.0	3.8	---	---	---	---	---	---
2	GW190806_033721	58.4	5.6	5.5	52.8	0.041	0.26	---	---	---
3	GW190524_134109	60.0	3.6	4.0	---	---	---	53.8	0.015	0.27
4	GW191113_103541	50.8	12.9	11.8	53.0	0.005	0.050	61.4	Veto	---
5	GW190615_030234	65.9	1.5	7.1	---	---	---	---	---	---
6	GW190604_103812	46.8	18.0	2.9	---	---	---	---	---	---
7	GW191228_195619	98.9	8.1	2.8	---	---	---	69.1	Veto	---
8	GW200304_172806	52.5	10.4	6.1	---	---	---	63.0	0.012	0.11
9	GW190530_030659	60.0	3.2	7.3	62.5	0.016	0.15	61.6	0.011	0.21
10	GW190511_163209	46.9	35.4	7.3	---	---	---	---	---	---
11	GW200210_100022	53.7	7.9	3.5	53.8	0.041	0.32	61.5	0.26	0.47
12	GW200301_211019	60.9	8.3	5.6	68.7	0.050	0.24	70.1	0.011	0.10
13	GW190911_195101	65.7	12.6	2.3	---	---	---	---	---	---
14	GW190530_133833	53.3	10.8	5.8	---	---	---	---	---	---

TABLE VI. Same as Table II but for candidates found with $p_{\text{astro}} > 10^{-3}$ which overlap with the new events reported in the IAS (2, 2)-only searches: [10, 40]. As we raised our ρ^2 bar for collecting triggers in the HM search, the following events from (2, 2)-only IAS searches were outside the domain of our search: GW190718_160159, GW191225_014544, GW200225_075134, GW191117_112541, GW200323_135352.

(O3a) Name	Bank	Best fit template				ρ_{H}^2	ρ_{L}^2	IFAR (yr)	p_{astro}
		$m_1^{\text{det}}(M_{\odot})$	$m_2^{\text{det}}(M_{\odot})$	χ_{eff}	\mathcal{M}_c				
GW190711_030756	7,1	79.9	23.4	-0.10	36.3	32.5	68.9	38.7	0.99
GW190707_083226	7,1	65.6	30.3	-0.41	38.3	49.4	40.2	0.30	0.81
GW190818_232544	8,1	129	61.2	0.51	76.3	47.9	35.8	0.23	0.77
GW190906_054335	7,1	80.2	14.0	-0.051	27.3	27.3	43.6	0.064	0.55
GW190814_192009	11,0	241	38.7	0.57	78.1	32.9	36.9	0.019	0.31
GW190821_124821	0,1	9.0	4.6	-0.38	5.6	31.1	55.3	0.012	0.23
GW190704_104834	0,0	6.8	4.1	0.18	4.6	52.2	42.5	0.009	0.18
GW190920_113516	0,0	5.9	4.0	0.51	4.2	29.6	56.0	0.007	0.15
GW190910_012619	5,0	47.8	3.0	-0.51	9.0	50.1	31.8	< 0.001	0.008
(O3b) Name	Bank	$m_1^{\text{det}}(M_{\odot})$	$m_2^{\text{det}}(M_{\odot})$	χ_{eff}	\mathcal{M}_c	ρ_{H}^2	ρ_{L}^2	IFAR (yr)	p_{astro}
GW200109_195634	10,0	176	98.9	0.60	114	42.6	36.2	0.23	0.78
GW191228_085854	0,2	15.6	4.7	-0.56	7.2	33.3	50.7	0.054	0.50
GW200316_235947	0,0	7.4	4.2	-0.20	4.8	45.9	39.7	0.002	0.028

TABLE VII. Same as Table I but for candidates found with $0.1 < p_{\text{astro}} < 0.5$ and $\text{IFAR} > 1$ per bank for the respective observing run (O3a or O3b). The significance of these events depends on the assumed astrophysical prior.

Candidate	Bank	Best fit template				ρ_{H}^2	ρ_{L}^2	IFAR (yr)		p_{astro}
		$m_1^{\text{det}} (M_{\odot})$	$m_2^{\text{det}} (M_{\odot})$	χ_{eff}	\mathcal{M}_c			per bank	overall	
GW190708_211916	8,1	107	17.9	0.20	35.5	42.1	32.8	0.46	0.049	0.50
GW190907_111633	12,0	318	33.7	0.82	81.1	27.1	42.3	0.45	0.046	0.48
GW191121_042622	13,0	250	148	0.76	166	24.5	44.0	0.51	0.038	0.42
GW190810_180039	6,2	68.2	32.8	0.18	40.7	33.1	37.4	0.36	0.028	0.38
GW200304_182240	11,0	278	15.8	0.85	49.3	36.4	29.9	0.26	0.031	0.37
GW200104_184028	8,1	65.8	57.0	-0.94	53.3	41.1	34.1	0.33	0.030	0.37
GW191127_114537	13,0	291	104	0.74	147	25.5	47.5	0.39	0.030	0.36
GW190423_083253	10,0	183	32.6	0.48	62.8	35.7	31.0	0.16	0.022	0.33
GW200324_083227	7,1	166	23.6	0.95	50.2	45.0	43.3	0.34	0.026	0.33
GW200312_093903	11,0	223	13.7	0.71	41.3	34.5	34.0	0.20	0.024	0.32
GW200308_231646	8,1	113	73.9	0.33	79.2	31.6	35.9	0.27	0.024	0.32
GW190620_221103	7,1	114	76.4	0.95	80.8	38.2	31.3	0.28	0.019	0.30
GW200211_113417	11,0	235	13.5	0.75	41.8	36.7	31.9	0.18	0.022	0.30
GW200128_115507	8,1	107	72.5	0.17	76.4	34.1	36.0	0.24	0.021	0.29
GW190606_061230	0,2	10.8	8.1	-0.38	8.1	31.8	43.6	0.36	0.018	0.29
GW190928_163629	4,2	80.5	18.1	0.64	31.6	32.2	36.5	0.27	0.016	0.27
GW200208_194804	13,0	333	31.4	0.84	79.3	31.1	31.1	0.26	0.019	0.27
GW200217_211137	9,0	121	78.5	0.036	84.4	29.6	36.7	0.17	0.019	0.27
GW190426_180646	7,1	109	14.5	0.53	31.7	26.2	49.5	0.23	0.015	0.27
GW200307_084747	9,0	111	6.4	-0.18	19.8	25.0	39.7	0.15	0.017	0.25
GW200216_200717	8,1	89.4	65.3	0.54	66.4	33.7	32.7	0.18	0.016	0.24
GW190403_061805	6,0	95.9	8.8	0.70	22.5	23.1	55.6	0.17	0.013	0.23
GW200226_083409	6,2	64.6	29.5	-0.20	37.5	38.1	32.5	0.17	0.014	0.21
GW190521_071322	7,1	91.4	13.4	0.48	28.1	31.3	42.5	0.16	0.010	0.19
GW190908_161547	7,1	91.7	56.4	0.32	62.2	48.4	36.3	0.16	0.010	0.19
GW190911_021724	4,2	42.9	24.8	-0.022	28.2	31.3	38.9	0.17	0.010	0.19
GW200303_074125	7,1	83.1	74.3	0.47	68.4	30.0	38.6	0.17	0.012	0.19
GW190526_231941	7,1	94.0	13.4	0.34	28.5	28.9	57.7	0.15	0.009	0.18
GW200319_022728	8,1	65.8	57.0	-0.94	53.3	25.6	44.4	0.13	0.012	0.18
GW200303_083614	0,1	8.2	5.9	0.24	6.0	34.1	51.4	0.21	0.011	0.18
GW191206_163102	13,0	371	24.9	0.90	72.5	29.4	41.8	0.15	0.011	0.17
GW191203_034221	3,1	37.7	4.1	0.025	9.8	30.2	44.4	1.3	0.011	0.17
GW200305_225311	3,1	29.7	6.2	-0.46	11.1	46.1	45.1	1.2	0.010	0.16
GW200126_225208	7,1	104	38.5	0.80	53.8	40.2	37.8	0.14	0.010	0.16
GW191209_143052	0,1	8.9	4.7	-0.27	5.6	35.9	47.8	0.17	0.010	0.16
GW200128_113935	4,2	62.1	18.3	0.37	28.3	45.1	30.6	0.17	0.010	0.16
GW200201_030733	4,2	78.8	38.8	0.76	47.5	36.7	41.4	0.16	0.010	0.15
GW200202_160037	4,2	46.8	38.7	-0.21	37.0	34.8	35.2	0.16	0.009	0.15
GW191209_191159	14,0	323	63.0	0.58	117	29.4	37.6	0.29	0.009	0.15
GW200212_101822	0,3	14.5	7.2	-0.92	8.8	53.9	37.1	0.14	0.008	0.13
GW190911_025827	14,0	265	112	0.21	147	24.2	54.3	0.22	0.006	0.13
GW200303_013439	0,2	13.8	6.9	0.48	8.4	32.9	43.1	0.14	0.008	0.13
GW190802_095334	5,2	64.8	6.9	0.24	16.6	29.0	47.5	1.8	0.006	0.12
GW191203_121111	14,0	356	23.4	0.70	68.6	28.9	35.9	0.25	0.008	0.12
GW190928_223455	2,0	53.4	9.1	0.51	17.9	33.8	39.9	0.21	0.005	0.10
GW191227_044656	14,0	361	32.5	0.60	83.6	24.9	38.1	0.21	0.006	0.10

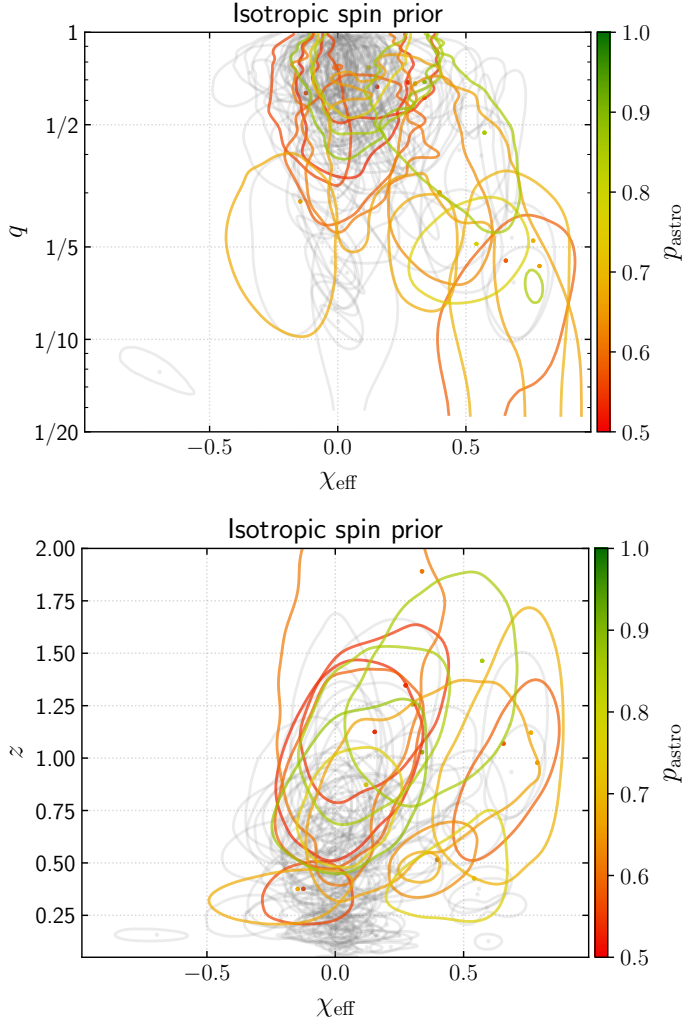


FIG. 7. Same as Fig. 1, but showing the 2D parameter estimation contours for χ_{eff} alongside mass ratio (redshift) in the top (bottom) panel.

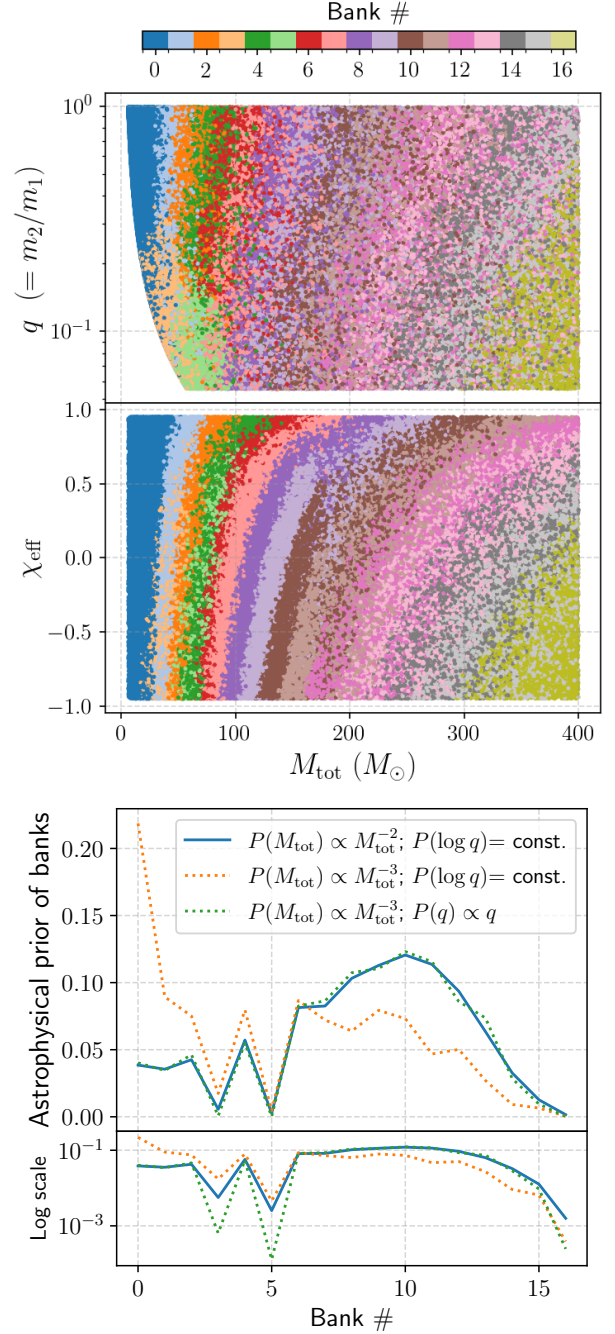


FIG. 8. **Top:** Physical parameters corresponding to each bank (this panel is taken from our companion paper [1] and is shown here for reference). **Bottom:** Prior probability corresponding to the number of events expected in individual banks. Solid line corresponds to our fiducial astrophysical prior in Section II D. For reference, we compare the probabilities for a different mass and mass ratio distribution in dotted lines. Note that Banks 3 and 5 show dips because they primarily include low- q systems which have a smaller observable distance due to their lower chirp masses. The decrement seen for the high-mass banks is primarily due to the binary merger starting to fall out of band at lower frequencies (there is also a contribution from the power law mass prior)^a.

^a One particularly notable example of a candidate which got down-weighted due to its prior is GW190805_100753. It was found in Bank # 16 with IFAR = 10 yr within the bank. However, after combining all banks, its IFAR became 1.3×10^{-4} yr and hence it is not present in our final list.

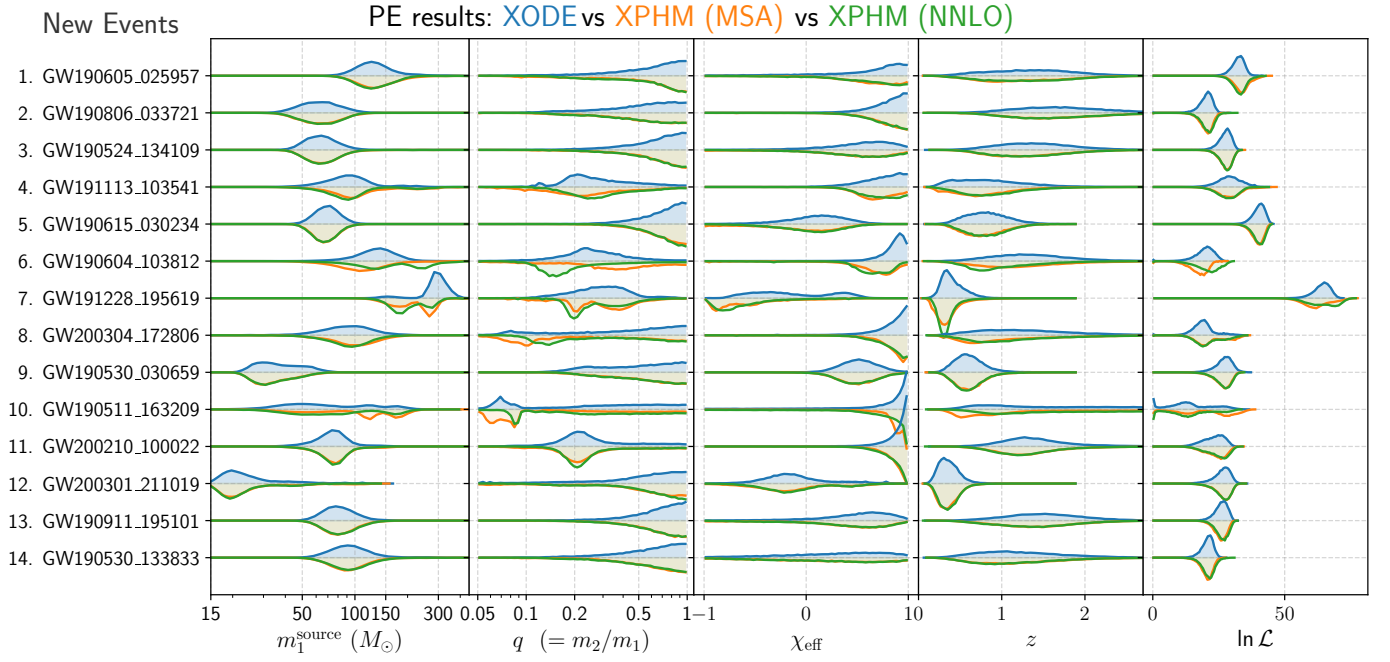


FIG. 9. Similar to Fig. 3 but comparing our fiducial PE results in the main paper (using IMRPhenomXODE [47]) to the PE results from IMRPhenomXPHM (under the two cases of MSA [49] and NNLO [50] approximations).

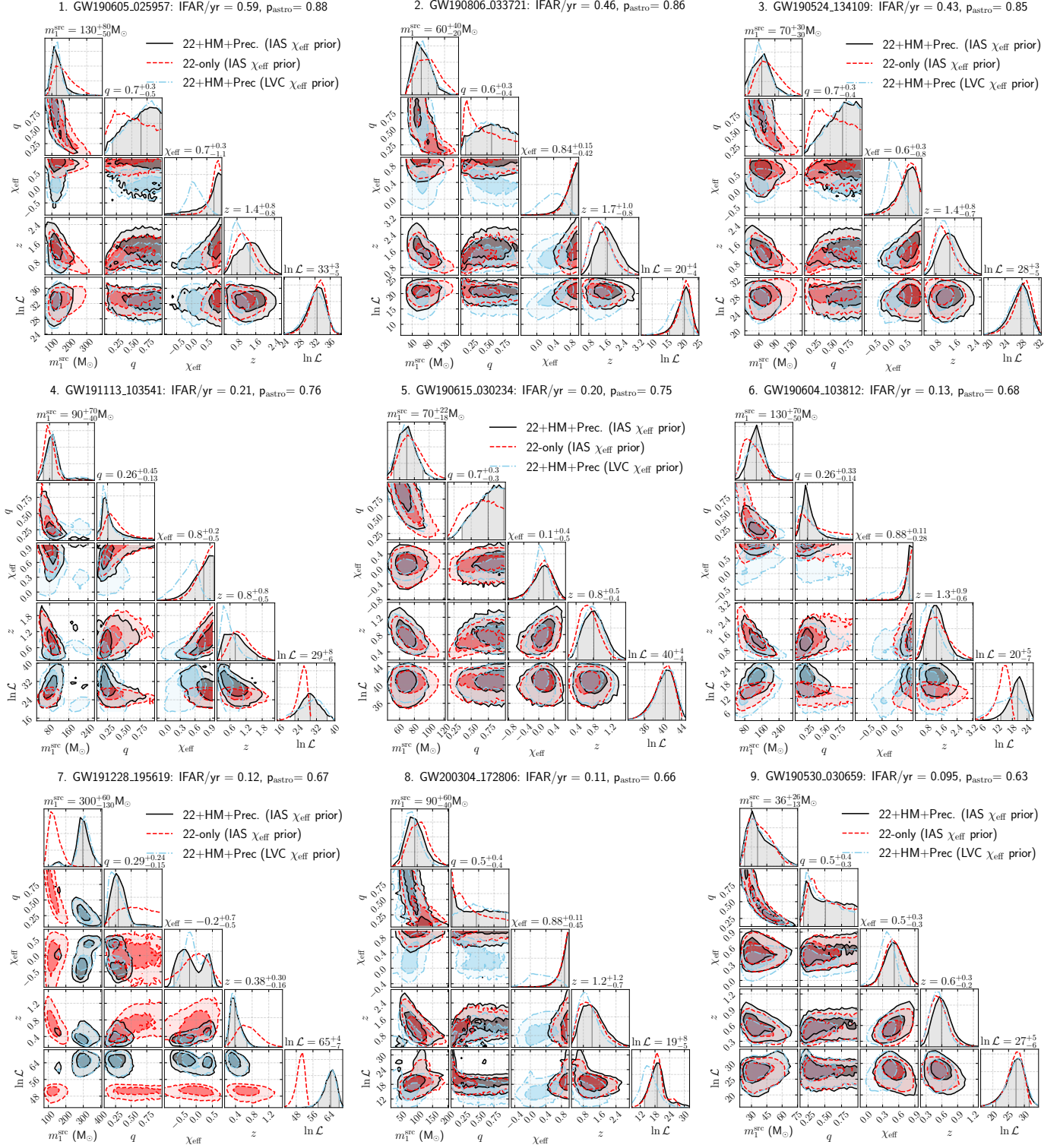


FIG. 10. Corner plots for the first nine of the new candidate events reported in the Table I (ranked by p_{astro} values). The marginalized values shown on the top of each column in the panels correspond to 90% confidence intervals for our fiducial PE (shown in black) for the flat-in- χ_{eff} prior (for the isotropic in component spin prior, we show the results in cyan). Our fiducial PE includes waveforms with HM and precession, but we also show in red the PE results with (2, 2)-only aligned-spin waveforms. Note that events # 4, 6, 7 have significant support for HM and precession. We further discuss the interesting astrophysical properties of these candidate events in Section IV.

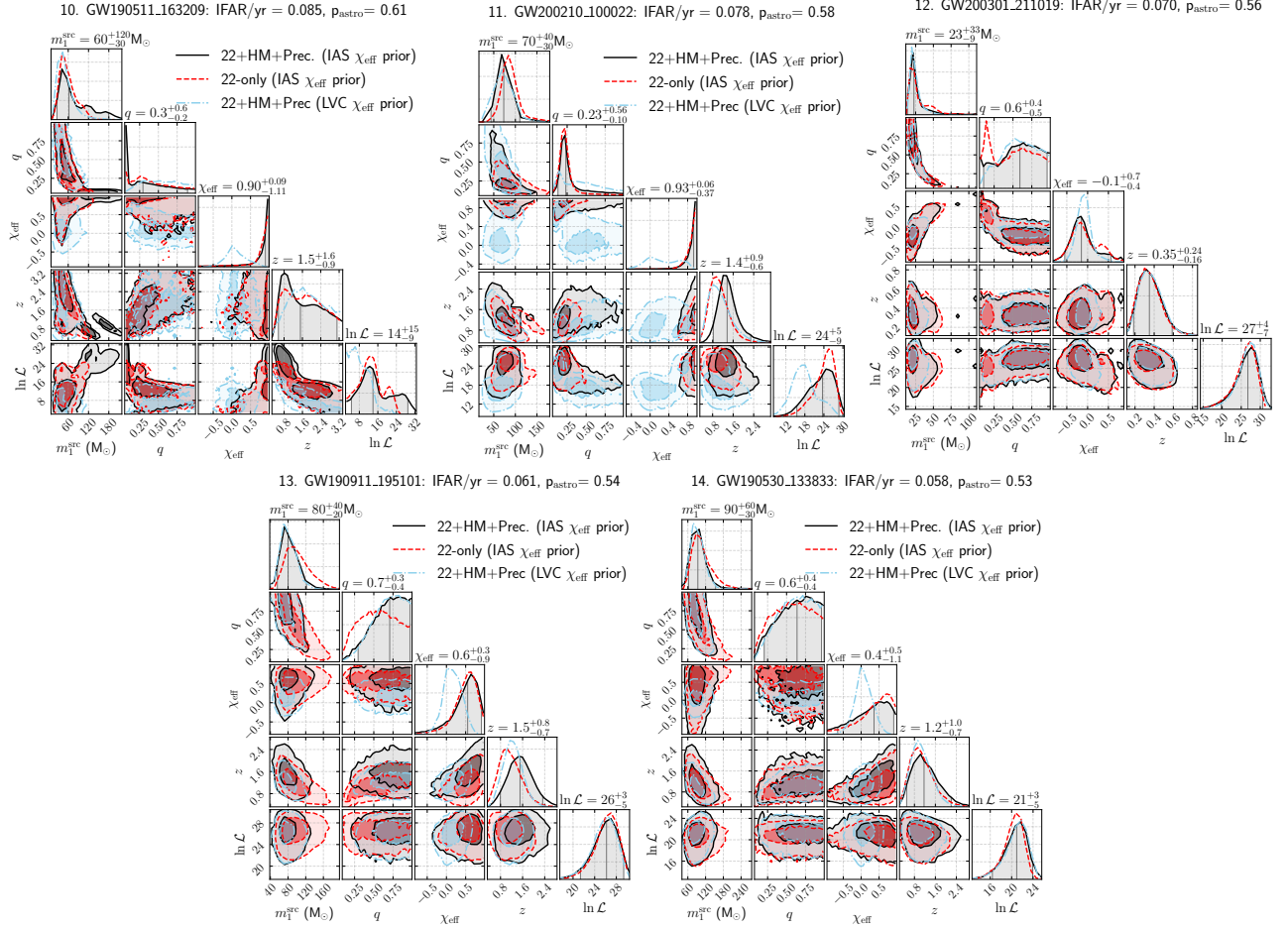


FIG. 11. Same as Fig. 10 but for events numbered 9–14 in the Table I. Note that event # 11 has significant support for HM and precession.

- [1] D. Wadekar, T. Venumadhav, A. K. Mehta, J. Roulet, *et al.*, arXiv e-prints, arXiv:2310.15233 (2023), arXiv:2310.15233 [gr-qc].
- [2] D. Wadekar *et al.*, in preparation (2023).
- [3] B. P. Abbott *et al.* (LIGO Scientific Collaboration and Virgo Collaboration), *Phys. Rev. X* **6**, 041015 (2016).
- [4] B. P. Abbott *et al.* (LIGO Scientific, Virgo), *Phys. Rev. X* **9**, 031040 (2019), arXiv:1811.12907 [astro-ph.HE].
- [5] R. Abbott *et al.*, *Physical Review X* **11**, 021053 (2021), arXiv:2010.14527 [gr-qc].
- [6] The LIGO Scientific Collaboration, the Virgo Collaboration, *et al.*, arXiv e-prints, arXiv:2108.01045 (2021), arXiv:2108.01045 [gr-qc].
- [7] R. Abbott *et al.* (LIGO Scientific, VIRGO, KAGRA), (2021), arXiv:2111.03606 [gr-qc].
- [8] T. Venumadhav, B. Zackay, J. Roulet, L. Dai, and M. Zaldarriaga, *Phys. Rev. D* **100**, 023011 (2019), arXiv:1902.10341 [astro-ph.IM].
- [9] T. Venumadhav, B. Zackay, J. Roulet, L. Dai, and M. Zaldarriaga, *Phys. Rev. D* **101**, 083030 (2020), arXiv:1904.07214 [astro-ph.HE].
- [10] S. Olsen, T. Venumadhav, J. Mushkin, J. Roulet, B. Zackay, and M. Zaldarriaga, *Phys. Rev. D* **106**, 043009 (2022).
- [11] A. H. Nitz, C. Capano, A. B. Nielsen, S. Reyes, R. White, D. A. Brown, and B. Krishnan, *The Astrophysical Journal* **872**, 195 (2019).
- [12] A. H. Nitz, T. Dent, G. S. Davies, S. Kumar, *et al.*, *Astrophys. J.* **891**, 123 (2020), arXiv:1910.05331 [astro-ph.HE].
- [13] A. H. Nitz, C. D. Capano, S. Kumar, Y.-F. Wang, *et al.*, arXiv e-prints, arXiv:2105.09151 (2021), arXiv:2105.09151 [astro-ph.HE].
- [14] A. H. Nitz, S. Kumar, Y.-F. Wang, S. Kastha, *et al.*, “4-OGC: Catalog of gravitational waves from compact-binary mergers,” (2021), arXiv:2112.06878 [astro-ph.HE].
- [15] H. S. Chia, T. D. P. Edwards, D. Wadekar, A. Zimmerman, *et al.*, arXiv e-prints, arXiv:2306.00050 (2023), arXiv:2306.00050 [gr-qc].
- [16] M. Vallisneri, J. Kanner, R. Williams, A. Weinstein, and B. Stephens, in *Journal of Physics Conference Series*, Journal of Physics Conference Series, Vol. 610 (2015) p. 012021, arXiv:1410.4839 [gr-qc].
- [17] J. Roulet, S. Olsen, J. Mushkin, T. Islam, T. Venumadhav, B. Zackay, and M. Zaldarriaga, *Phys. Rev. D* **106**, 123015 (2022), arXiv:2207.03508 [gr-qc].
- [18] K. S. Thorne, *Rev. Mod. Phys.* **52**, 299 (1980).
- [19] Y. Pan, A. Buonanno, M. Boyle, L. T. Buchman, L. E. Kidder, H. P. Pfeiffer, and M. A. Scheel, *Phys. Rev. D* **84**, 124052 (2011), arXiv:1106.1021 [gr-qc].
- [20] C. Mills and S. Fairhurst, *Phys. Rev. D* **103**, 024042 (2021), arXiv:2007.04313 [gr-qc].
- [21] V. Varma, P. Ajith, S. Husa, J. C. Bustillo, M. Hannam, and M. Pürrer, *Phys. Rev. D* **90**, 124004 (2014), arXiv:1409.2349 [gr-qc].
- [22] R. Abbott, LIGO Scientific Collaboration, and Virgo Collaboration, *Phys. Rev. D* **102**, 043015 (2020), arXiv:2004.08342 [astro-ph.HE].
- [23] R. Abbott *et al.*, *ApJ* **896**, L44 (2020), arXiv:2006.12611 [astro-ph.HE].
- [24] S. Kastha, A. Gupta, K. G. Arun, B. S. Sathyaprakash, and C. Van Den Broeck, *Phys. Rev. D* **98**, 124033 (2018), arXiv:1809.10465 [gr-qc].
- [25] S. Kastha, A. Gupta, K. G. Arun, B. S. Sathyaprakash, and C. Van Den Broeck, *Phys. Rev. D* **100**, 044007 (2019), arXiv:1905.07277 [gr-qc].
- [26] S. Dhanpal, A. Ghosh, A. K. Mehta, P. Ajith, and B. S. Sathyaprakash, *Phys. Rev. D* **99**, 104056 (2019), arXiv:1804.03297 [gr-qc].
- [27] T. Islam, A. K. Mehta, A. Ghosh, V. Varma, P. Ajith, and B. S. Sathyaprakash, *Phys. Rev. D* **101**, 024032 (2020), arXiv:1910.14259 [gr-qc].
- [28] C. D. Capano, M. Cabero, J. Westerweck, J. Abedi, *et al.*, “Observation of a multimode quasi-normal spectrum from a perturbed black hole,” (2021), arXiv:2105.05238 [gr-qc].
- [29] L. London, S. Khan, E. Fauchon-Jones, C. García, *et al.*, *Phys. Rev. Lett.* **120**, 161102 (2018), arXiv:1708.00404 [gr-qc].
- [30] C. García-Quirós, M. Colleoni, S. Husa, H. Estellés, *et al.*, *Phys. Rev. D* **102**, 064002 (2020), arXiv:2001.10914 [gr-qc].
- [31] A. K. Mehta, C. K. Mishra, V. Varma, and P. Ajith, *Phys. Rev. D* **96**, 124010 (2017), arXiv:1708.03501 [gr-qc].
- [32] K. Chandra, J. Calderón Bustillo, A. Pai, and I. Harry, arXiv e-prints, arXiv:2207.01654 (2022), arXiv:2207.01654 [gr-qc].
- [33] I. Harry, J. C. Bustillo, and A. Nitz, *Phys. Rev. D* **97**, 023004 (2018).
- [34] S. Schmidt, B. Gadre, and S. Caudill, arXiv e-prints, arXiv:2302.00436 (2023), arXiv:2302.00436 [gr-qc].
- [35] C. Capano, Y. Pan, and A. Buonanno, *Physical Review D* **89** (2014), 10.1103/physrevd.89.102003.
- [36] A. H. Nitz, T. Dent, T. Dal Canton, S. Fairhurst, and D. A. Brown, *ApJ* **849**, 118 (2017), arXiv:1705.01513 [gr-qc].
- [37] J. Roulet *et al.*, in preparation (2023).
- [38] B. Zackay, T. Venumadhav, J. Roulet, L. Dai, and M. Zaldarriaga, *Phys. Rev. D* **104**, 063034 (2021).
- [39] B. P. Abbott *et al.* (LIGO Scientific, Virgo), *Phys. Rev. D* **93**, 122003 (2016), arXiv:1602.03839 [gr-qc].
- [40] A. K. Mehta, S. Olsen, D. Wadekar, J. Roulet, *et al.*, arXiv e-prints, arXiv:2311.06061 (2023), arXiv:2311.06061 [gr-qc].
- [41] G. Pratten, S. Husa, C. Garcia-Quiros, M. Colleoni, A. Ramos-Buades, H. Estelles, and R. Jaume, *Phys. Rev. D* **102**, 064001 (2020), arXiv:2001.11412 [gr-qc].
- [42] M. Fishbach and D. E. Holz, *ApJ* **851**, L25 (2017), arXiv:1709.08584 [astro-ph.HE].
- [43] J. Roulet, L. Dai, T. Venumadhav, B. Zackay, and M. Zaldarriaga, *Phys. Rev. D* **99**, 123022 (2019).
- [44] J. U. Lange, “Nautilus: boosting bayesian importance nested sampling with deep learning,” (2023), arXiv:2306.16923 [astro-ph.IM].
- [45] B. Zackay, L. Dai, and T. Venumadhav, (2018), arXiv:1806.08792 [astro-ph.IM].
- [46] P. A. R. Ade *et al.* (Planck), *Astron. Astrophys.* **594**, A13 (2016), arXiv:1502.01589 [astro-ph.CO].
- [47] H. Yu, J. Roulet, T. Venumadhav, B. Zackay, and M. Zaldarriaga, *Phys. Rev. D* **108**, 064059 (2023),

- arXiv:2306.08774 [gr-qc].
- [48] G. Pratten, C. García-Quiros, M. Colleoni, A. Ramos-Buades, *et al.*, *Phys. Rev. D* **103**, 104056 (2021).
- [49] K. Chatziioannou, A. Klein, N. Yunes, and N. Cornish, *Phys. Rev. D* **95**, 104004 (2017), arXiv:1703.03967 [gr-qc].
- [50] M. Hannam, P. Schmidt, A. Bohé, L. Haegel, *et al.*, *Phys. Rev. Lett.* **113**, 151101 (2014), arXiv:1308.3271 [gr-qc].
- [51] T. Islam, A. Vajpeyi, F. H. Shaik, C.-J. Haster, *et al.*, arXiv e-prints, arXiv:2309.14473 (2023), arXiv:2309.14473 [gr-qc].
- [52] S. Sachdev, S. Caudill, H. Fong, R. K. L. Lo, *et al.*, (2019), arXiv:1901.08580v1 [gr-qc].
- [53] S. A. Usman, A. H. Nitz, I. W. Harry, C. M. Biwer, *et al.*, *Classical and Quantum Gravity* **33**, 215004 (2016), arXiv:1508.02357 [gr-qc].
- [54] N. Andres, M. Assiduo, F. Aubin, R. Chierici, *et al.*, *Classical and Quantum Gravity* **39**, 055002 (2022).
- [55] S. Klimentko, G. Vedovato, M. Drago, F. Salemi, *et al.*, *Phys. Rev. D* **93**, 042004 (2016).
- [56] R. Abbott *et al.* (LIGO Scientific Collaboration and Virgo Collaboration), *Phys. Rev. Lett.* **125**, 101102 (2020).
- [57] J. E. Greene, J. Strader, and L. C. Ho, *ARA&A* **58**, 257 (2020), arXiv:1911.09678 [astro-ph.GA].
- [58] G. Fragione, I. Ginsburg, and B. Kocsis, *ApJ* **856**, 92 (2018), arXiv:1711.00483 [astro-ph.GA].
- [59] P. Marchant and T. Moriya, *Astron. Astrophys.* **640**, L18 (2020), arXiv:2007.06220 [astro-ph.HE].
- [60] R. Farmer, M. Renzo, S. E. de Mink, P. Marchant, and S. Justham, (2019), 10.3847/1538-4357/ab518b, arXiv:1910.12874 [astro-ph.SR].
- [61] A. K. Mehta, A. Buonanno, J. Gair, M. C. Miller, *et al.*, *Astrophys. J.* **924**, 39 (2022), arXiv:2105.06366 [gr-qc].
- [62] D. D. Hendriks, L. A. C. van Son, M. Renzo, R. G. Izzard, and R. Farmer, *MNRAS* (2023), 10.1093/mnras/stad2857, arXiv:2309.09339 [astro-ph.HE].
- [63] R. Abbott *et al.* (KAGRA, VIRGO, LIGO Scientific), *Phys. Rev. X* **13**, 011048 (2023), arXiv:2111.03634 [astro-ph.HE].
- [64] J. Roulet, H. S. Chia, S. Olsen, L. Dai, T. Venumadhav, B. Zackay, and M. Zaldarriaga, *Phys. Rev. D* **104**, 083010 (2021).
- [65] O. Anagnostou, M. Trenti, and A. Melatos, (2020), arXiv:2010.06161 [astro-ph.HE].
- [66] G. Fragione, A. Loeb, and F. A. Rasio, *Astrophys. J. Lett.* **902**, L26 (2020), arXiv:2009.05065 [astro-ph.GA].
- [67] D. Veske, A. G. Sullivan, Z. Márka, I. Bartos, *et al.*, *Astrophys. J. Lett.* **907**, L48 (2021), arXiv:2011.06591 [astro-ph.HE].
- [68] G. Fragione, B. Kocsis, F. A. Rasio, and J. Silk, (2021), arXiv:2107.04639 [astro-ph.GA].
- [69] H. Tagawa, Z. Haiman, I. Bartos, and B. Kocsis, *ApJ* **899**, 26 (2020), arXiv:2004.11914 [astro-ph.HE].
- [70] J. Samsing, I. Bartos, D. J. D’Orazio, Z. Haiman, *et al.*, *Nature* **603**, 237 (2022), arXiv:2010.09765 [astro-ph.HE].
- [71] M. Fishbach, D. E. Holz, and W. M. Farr, *ApJ* **863**, L41 (2018), arXiv:1805.10270 [astro-ph.HE].
- [72] P. Madau and M. Dickinson, *ARA&A* **52**, 415 (2014), arXiv:1403.0007 [astro-ph.CO].
- [73] M. Mapelli, Y. Bouffanais, F. Santoliquido, M. Arca Sedda, and M. C. Artale, *MNRAS* **511**, 5797 (2022), arXiv:2109.06222 [astro-ph.HE].
- [74] L. A. C. van Son, S. E. de Mink, T. Callister, S. Justham, *et al.*, *ApJ* **931**, 17 (2022), arXiv:2110.01634 [astro-ph.HE].
- [75] I. Mandel and S. E. de Mink, *Monthly Notices of the Royal Astronomical Society* **458**, 2634 (2016).
- [76] M. Mapelli, N. Giacobbo, F. Santoliquido, and M. C. Artale, *MNRAS* **487**, 2 (2019), arXiv:1902.01419 [astro-ph.HE].
- [77] S. Biscoveanu, T. A. Callister, C.-J. Haster, K. K. Y. Ng, S. Vitale, and W. M. Farr, *ApJ* **932**, L19 (2022), arXiv:2204.01578 [astro-ph.HE].
- [78] D. Kushnir, M. Zaldarriaga, J. A. Kollmeier, and R. Waldman, *MNRAS* **462**, 844 (2016), arXiv:1605.03839 [astro-ph.HE].
- [79] M. Zaldarriaga, D. Kushnir, and J. A. Kollmeier, *MNRAS* **473**, 4174 (2018), arXiv:1702.00885 [astro-ph.HE].
- [80] K. K. Y. Ng, S. Vitale, A. Zimmerman, K. Chatziioannou, D. Gerosa, and C.-J. Haster, *Phys. Rev. D* **98**, 083007 (2018), arXiv:1805.03046 [gr-qc].
- [81] J. Roulet and M. Zaldarriaga, *Monthly Notices of the Royal Astronomical Society* **484**, 4216–4229 (2019).
- [82] C. L. Rodriguez, S. Chatterjee, and F. A. Rasio, *Phys. Rev. D* **93**, 084029 (2016), arXiv:1602.02444 [astro-ph.HE].
- [83] C. L. Rodriguez, M. Zevin, P. Amaro-Seoane, S. Chatterjee, K. Kremer, F. A. Rasio, and C. S. Ye, *Phys. Rev. D* **100**, 043027 (2019), arXiv:1906.10260 [astro-ph.HE].
- [84] N. Ivanova, S. Justham, X. Chen, O. De Marco, *et al.*, *A&A Rev.* **21**, 59 (2013), arXiv:1209.4302 [astro-ph.HE].
- [85] K. A. Postnov and L. R. Yungelson, *Living Reviews in Relativity* **17**, 3 (2014), arXiv:1403.4754 [astro-ph.HE].
- [86] F. S. Broekgaarden, S. Stevenson, and E. Thrane, *ApJ* **938**, 45 (2022), arXiv:2205.01693 [astro-ph.HE].
- [87] E. Payne, C. Talbot, and E. Thrane, *Phys. Rev. D* **100**, 123017 (2019).
- [88] B. Zackay, T. Venumadhav, L. Dai, J. Roulet, and M. Zaldarriaga, *Phys. Rev. D* **100**, 023007 (2019), arXiv:1902.10331 [astro-ph.HE].
- [89] J. Roulet, T. Venumadhav, B. Zackay, L. Dai, and M. Zaldarriaga, *Physical Review D* **102** (2020), 10.1103/physrevd.102.123022.
- [90] S. Khan, S. Husa, M. Hannam, F. Ohme, M. Pürrer, X. J. Forteza, and A. Bohé, *Physical Review D* **93** (2016), 10.1103/physrevd.93.044007.
- [91] S. Fairhurst, C. Mills, M. Colpi, R. Schneider, A. Sesana, A. Trinca, and R. Valiante, arXiv e-prints, arXiv:2310.18158 (2023), arXiv:2310.18158 [astro-ph.HE].
- [92] M. Maggiore *et al.*, *JCAP* **03**, 050 (2020), arXiv:1912.02622 [astro-ph.CO].
- [93] M. Evans *et al.*, arXiv e-prints, arXiv:2306.13745 (2023), arXiv:2306.13745 [astro-ph.IM].
- [94] S. Kawamura *et al.*, (2020), 10.48550/ARXIV.2006.13545.
- [95] P. Amaro-Seoane *et al.*, arXiv e-prints, arXiv:1702.00786 (2017), arXiv:1702.00786 [astro-ph.IM].
- [96] T. Akutsu *et al.* (KAGRA), *PTEP* **2021**, 05A101 (2021), arXiv:2005.05574 [physics.ins-det].
- [97] C. Zhang, N. Dai, and D. Liang, *Phys. Rev. D* **108**, 044076 (2023), arXiv:2306.13871 [gr-qc].
- [98] V. Baibhav, E. Berti, and V. Cardoso, *Phys. Rev. D* **101**, 084053 (2020), arXiv:2001.10011 [gr-qc].